Ocean Modelling 100 (2016) 57–77

Contents lists available at ScienceDirect

Ocean Modelling

journal homepage: www.elsevier.com/locate/ocemod

Energy-optimal path planning by stochastic dynamically orthogonal level-set optimization

Deepak N. Subramani*, Pierre F.J. Lermusiaux*

Department of Mechanical Engineering, Massachusetts Institute of Technology, 77 Mass. Ave., Cambridge, MA 02139, United States

ARTICLE INFO

Article history:
Received 18 September 2015
Revised 29 January 2016
Accepted 31 January 2016
Available online 9 February 2016

Keywords:
Path planning
Stochastic optimization
Dynamically orthogonal level-set equations
Reachability
Science of autonomy
Energy-optimal

ABSTRACT

A stochastic optimization methodology is formulated for computing energy-optimal paths from among time-optimal paths of autonomous vehicles navigating in a dynamic flow field. Based on partial differential equations, the methodology rigorously leverages the level-set equation that governs time-optimal reachability fronts for a given relative vehicle-speed function. To set up the energy optimization, the relative vehicle-speed and headings are considered to be stochastic and new stochastic Dynamically Orthogonal (DO) level-set equations are derived. Their solution provides the distribution of time-optimal reachability fronts and corresponding distribution of time-optimal paths. An optimization is then performed on the vehicle's energy-time joint distribution to select the energy-optimal paths for each arrival time, among all stochastic time-optimal paths for that arrival time. Numerical schemes to solve the reduced stochastic DO level-set equations are obtained, and accuracy and efficiency considerations are discussed. These reduced equations are first shown to be efficient at solving the governing stochastic level-sets, in part by comparisons with direct Monte Carlo simulations. To validate the methodology and illustrate its accuracy, comparisons with *semi-analytical* energy-optimal path solutions are then completed. In particular, we consider the energy-optimal crossing of a canonical steady front and set up its *semi-analytical* solution using a energy-time nested nonlinear double-optimization scheme. We then showcase the inner workings and nuances of the energy-optimal path planning, considering different mission scenarios. Finally, we study and discuss results of energy-optimal missions in a wind-driven barotropic quasi-geostrophic double-gyre ocean circulation.

1. Introduction

The use of autonomous underwater vehicles (AUVs) including propelled vehicles, gliders, and surface crafts is growing in a wide range of applications such as oil and gas exploration, ocean floor mapping, search and rescue, security, and coastal and global ocean monitoring, conservation and forecasting (Stommel, 1989; Bachmayer et al., 2004; Bellingham and Rajan, 2007). Due to uncertainties, ocean sampling is often at the heart of such underwater operations. For coupled sampling and exploration missions (e.g., Bhatta et al., 2005; Curtin and Bellingham, 2009; Bahr et al., 2009; Ramp et al., 2009; Haley et al., 2009; Leonard et al., 2010; Schofield et al., 2010), long endurance and low energy cost are crucial requirements. Specifically, there is a need to increase the capability of vehicles to operate for long periods of time at sea, often either by developing more efficient power supplies (Bellingham and Rajan, 2007) or by utilizing the environment to reduce energy consumption (Webb et al., 2001). Similar needs arise in other applications where the environment can play a significant role such as in the navigation of land robots, drones, airplanes, etc. Conserving fuel by designing energy-efficient paths leads to cost savings, longer operational time, and environmental protection. In this work, we present a methodology based on stochastic level-set partial differential equations (PDEs) that rigorously predicts energy-optimal paths in deterministic dynamic flows. Although ocean applications are emphasized, the methodology is valid for a wider class of environments.

The task of designing a path for a mobile agent that navigates from a start point (s) to a desired final point (f) by optimizing one or more of the travel time, energy expended, data collected, and vehicle safety, is commonly referred to as path planning. It is an area of active research in many domains (e.g., Hwang and Ahuja, 1992; LaValle, 2006; Sheu and Xue, 1993; Latombe, 1991; Kavraki et al., 1996; Lermusiaux et al., 2015). In the ocean domain, the effect of dynamic currents on the motion of vehicles is significant.

* Corresponding author. Tel.: +16173245172; fax: +16173243541.
E-mail addresses: deepakns@mit.edu (D.N. Subramani), pierrel@mit.edu (P.F.J. Lermusiaux).

http://dx.doi.org/10.1016/j.ocemod.2016.01.006
1463-5003/

Fig. 1. Consider planning the path of a vehicle between $\mathbf{x_s}$ and $\mathbf{x_f}$ in a flow field $\mathbf{v}(\mathbf{x}, t)$. Our goal is to compute minimal energy paths (speed functions $F(\bullet)$ and headings $\hat{h}(\bullet)$), optimizing among the distribution of time-optimal paths for each $F(\bullet)$.

Typical propelled AUVs have an endurance of 12–25 h and speeds up to 5 knots, and typical gliders have an endurance of a few days to months and speeds up to 1 knot (Sherman et al., 2001; Rudnick et al., 2004; Schofield et al., 2007). As such strong currents can be comparable to the speed of propelled AUVs (Schmidt et al., 1996; Elisseeff et al., 1999) and common currents can be two-to-three times faster than glider speeds. The energy budget of gliders directly depends on flow conditions, the largest energy expenditure often being skin friction (Eriksen et al., 2001). For our energy-optimal planning, a main challenge is thus to develop accurate and efficient algorithms that intelligently utilize the favorable currents and avoid the adverse currents, so as to optimize endurance and energy consumption. Another challenge is to rigorously incorporate the variability of ocean fields, combining ocean modeling and observations with PDE-based optimization. This challenge is especially relevant for the case of vehicles that once deployed have little or no human interventions. As such, there is an opportunity to capitalize on ocean prediction systems (within their predictive capability) so as to forecast the energy-optimal paths even prior to the deployment of vehicles.

Our goal is to develop a rigorous and efficient methodology that computes energy-optimal relative speeds and headings for navigating between two locations in a dynamic flow field, optimizing from among time-optimal paths (see Fig. 1). Some of the questions that inspired our work include the following. Can energy-optimal paths in complex ocean currents be computed at all? Should this computation be posed as a stochastic PDE-based optimization problem? Can dynamic model-order reductions be employed? What are the overall accuracy and costs of the methodology? What are the energy-optimal paths in fundamental ocean flows? Even though path planning for robotic systems has received much attention (Latombe, 1991; LaValle, 2006; Lolla, 2012), answering such questions for large-dimensional, strong and unsteady ocean flows is challenging.

One type of AUV energy-optimization is based on the A* algorithm (Carroll et al., 1992; Garau et al., 2005). It was used by Garau et al. (2009) to reduce the energy consumption for gliders and by Lee et al. (2015) with an energy-based cost function considering environmental effects and a heuristic for a marine surface vehicle. However, the A* algorithm does not guarantee optimality when a heuristic is not available and its paths become infeasible in strong variable flows. Rapidly Exploring Random Trees (RRTs) (e.g., LaValle, 1998; Kuffner and LaValle, 2000) is a sampling-based method used to explore the workspace for navigating a robot quickly and uniformly. For underwater path planning, Tan et al. (2004) used RRTs to obtain an obstacle free path for an AUV, but without considering currents. Rao and Williams (2009) used RRTs to generate feasible paths for gliders and an A* search to identify a path from among RRT paths that minimizes an energy-based linear-speed cost heuristic. However, the authors report that the method is not capable of identifying minimum energy paths when the flow is strong. For more on RRTs, we refer to Bruce and Veloso, 2002; Melchior and Simmons, 2007; Jaillet et al., 2010; Yang et al., 2010; Karaman and Frazzoli, 2011. A related method using a kinematic-tree-based navigation planner was developed by Chakrabarty and Langelaan (2013) for UAVs in unsteady wind fields.

The above methods are discrete node-based graph methods. For path planning in continuous fields, fast marching methods can be used (Sethian, 1999a; 1999b), including anisotropic cost functions (Petres et al., 2007). However, they are limited to currents smaller than vehicle-speeds (Lolla et al., 2014c). Continuous wavefront expansion methods have also been used (Soulignac et al., 2009; Thompson et al., 2009; 2010). Path parameterization and an optimization on the path parameters has been successful in simulations for the Sicily channel (Alvarez et al., 2004). The authors obtain candidate paths and then optimize them through a genetic algorithm (GA), minimizing the energy required to overcome a cubic-velocity drag. However, the GA and other evolutionary algorithms (Chien-Chou et al., 2014) are not guaranteed to converge in finite time and not all assumptions are applicable to complex flows. Kruger et al. (2007) also employ a path parameterization but utilize a nonlinear optimization, with applications to Hudson River simulations. Their weighted cost function accounts for energy with variable engine thrust, obstacle avoidance, time of travel, and target visitation. Even though such nonlinear optimization does not have the drawbacks of evolutionary algorithms, they are constrained by the chosen path parameterization, which limits the generality of the method and can increase computational costs. Potential field techniques used to repel vehicles away from obstacles (Warren, 1990; Barraquand et al., 1992) were also combined with path parameterization and swarm optimization for energy-based path planning (Witt and Dunbabin, 2008). The authors still employed heuristics and ad-hoc refinements, with successful tests using forecasts for Brisbane's Moreton Bay.

In general, path planning problems are nonlinear optimal control problems (Bryson and Ho, 1975; McLain and Beard, 1998), which classically amount to solving 2-point boundary value problems. When the environmental flows are time-dependent fields, such problems are expensive and difficult to solve. Aghababa (2012) uses this approach for energy-optimal path planning by fixing a maximum time to reach and solving for a path that minimizes an energy cost that depends on nominal velocity to the power of 3/2. However, the author used evolutionary algorithms (GA and ant-colony optimization) and used simple test problems to evaluate their performance in comparison to conjugate gradient methods. An indirect external field algorithm for computing the optimal *time-to-go* and associated optimal feedback control loop is tested on a time-invariant double-gyre and Adriatic sea simulations by Rhoads et al. (2010). Sequential quadratic programming was used by Beylkin (2008) to optimize the path for a balloon moving in a windy atmosphere by minimizing an l_2-norm of the control. Inanc et al. (2005), Zhang et al. (2008) illustrated that the optimal energy-time-weighted paths computed by a heuristic *receding-horizon* nonlinear programming problem (NLP) method were close to paths along Lagrangian Coherent Structures (LCS) estimated from Monterey Bay HF-radar data. Hsieh et al. (2012), Michini et al. (2014) also successfully applied collaborative tracking of LCS in a double-gyre simulation, experimental flow tank data, and ocean data for the Santa Barbara Channel. Game theoretic considerations were used by Sun and Tsiotras (2015) to plan paths for pursuit–evasion games between two UAVs navigating in an external flow field.

Recently, a modified level-set PDE was obtained for time-optimal path planning of autonomous agents in any dynamic flow field. (Lolla et al., 2014b; 2014c; Lolla and Lermusiaux, 2016). This Hamilton–Jacobi (HJ) PDE governs exactly and efficiently the forward-in-time reachability front. To generate the time-optimal paths, a particle tracking equation is solved backward in time. These equations and a definition of level–sets are provided in Appendix A. Here, we extend this deterministic PDE–based methodology to a stochastic PDE–based optimization to compute minimum energy paths among time-optimal paths. A new idea is to introduce variable and stochastic vehicle–speeds, and to perform an optimization on the energy utilized by such vehicles as they navigate from start to end in a time-optimal fashion. The variable vehicle-speed allows for energy optimization. Another idea is to utilize dynamic model-order reduction and uncertainty quantification, the Dynamically Orthogonal (DO) equations, to integrate the level-set HJ PDE with stochastic vehicle-speeds. Specifically, we thus derive and apply novel DO equations for this stochastic level-set HJ PDE. Since sample-wise solutions of this stochastic PDE (S-PDE) are guaranteed to be time-optimal paths, minimizing the energy consumed among such time-optimal paths provides the energy optimal paths. Such an application of the DO method for probabilistic exploration to solve an optimization problem is attempted here for the first time. We note that the stochasticity in the problem comes from the vehicle-speed, and not the flow field which is deterministic in the present paper. Our applications show that the variable vehicle-speed optimized by our methodology intelligently utilizes the deterministic forecast currents thereby saving energy (e.g., turning the on-board engine to low speed when currents are favorable). In general, our S-PDE-based optimization solves for speed functions and paths that save the most energy for a set of arrival times.

In what follows, we first present the mathematical problem statement and a few remarks (Section 2). In Section 3, we develop the methodology and new stochastic DO level-set PDEs. Due to the non-polynomial nonlinearity in these S-PDEs, we derive three variants for these DO equations. In Section 4, we discuss numerical schemes, algorithms, and computational complexity. In Section 5, we perform a two step validation process. First, we show that the solutions of the stochastic DO level-set PDEs solve the original S-PDE correctly and discuss the computational advantages of the DO approach. Second, we validate the stochastic optimization by applying it to the planning of energy-optimal paths in a canonical flow that permits a semi-analytical solution. Our final application (Section 6) is to plan paths in a dynamical barotropic quasi-geostrophic double-gyre circulation.

2. Problem statement

Time-optimal path planning with given time-dependent vehicle speed. We start with time–optimal path planning and the HJ level-set equation (A.1) governing the reachability front (see Appendix A), but with a straightforward extension: the relative vehicle-speed $F(t)$ is given but time-dependent. Let us consider a vehicle with a relative *time-dependent* non-negative speed, i.e., $F(t) \geq 0$ navigating from a start point ($\mathbf{x_s}$) to an end point ($\mathbf{x_f}$) in $\Omega \subseteq \mathbb{R}^n$, an open set (see Fig. 1). The environmental flow is denoted by $\mathbf{v}(\mathbf{x}, t) : \Omega \times (0, \infty) \to \mathbb{R}^n$ and is assumed known. The reachability front is then governed by the HJ level-set equation as (A.1) but with $F = F(t)$, i.e.,

$$\frac{\partial \phi}{\partial t} + F(t)|\nabla \phi| + \mathbf{v}(\mathbf{x}, t) \cdot \nabla \phi = 0 \tag{1}$$

with the level-set ϕ initialized by a signed distance function from the starting point $\mathbf{x_s}$, i.e., $\phi(\mathbf{x}, 0) = |\mathbf{x} - \mathbf{x_s}|$. The backtracking equation for that given $F(t)$ then yields the time-optimal path, i.e.,

$$\frac{\mathrm{d}\mathbf{x}^*}{\mathrm{d}t} = -\mathbf{v}(\mathbf{x}^*, t) - F(t)\frac{\nabla \phi(\mathbf{x}^*, t)}{|\nabla \phi(\mathbf{x}^*, t)|}, \quad 0 \leq t \leq T(\mathbf{x_f}; F(t)) \quad \text{and} \quad \mathbf{x}^*(T) = \mathbf{x_f}. \tag{2}$$

To briefly explain this extension, consider a time $t > 0$ with the vehicle on the reachability front. From this instant, the vehicle travels at an instantaneous given (vehicle) speed $F(t)$ for a time interval dt. The reachability front (i.e., the zero level-set) evolves normal to itself with this instantaneous speed $F(t)$. The reachability front still remains optimal for this $F(t)$. For backtracking, the heading $\hat{h}(t)$ is normal to the zero level-set, which at the instant t, is independent of the instantaneous $F(t)$, and hence the same for all $F(t)$. For two different $F(t)$, the only difference is the rate at which the reachability front evolves normal to itself. Hence, for a given and variable $F(t)$, the solution of Eqs. (1) forward in time and (2) backward in time, yields the time–optimal path. Lolla and Lermusiaux (2016) provide a formal derivation accounting for generalized derivatives and viscosity solutions.

Energy-optimal path planning. The energy-optimal path planning problem for the vehicle navigating in Ω under the influence of $\mathbf{v}(\mathbf{x}, t)$ (Fig. 1) can be formulated as follows. The variable vehicle speed function $F(\bullet)$ is to be optimized for energy and time. The heading function $\hat{h}(\bullet)$ for the vehicle is optimized such that when navigated at any speed function $F(\bullet)$, the vehicle reaches $\mathbf{x_f}$ in optimal time $T(\mathbf{x_f}; F(\bullet))$. Among all of these functions $F(\bullet)$, we seek the $F(t)$ that minimizes the energy cost function E, i.e.,

$$\min_{F(\bullet)} \left\{ E(\bullet) \equiv \int_0^{T(\mathbf{x_f}; F(\bullet))} p(t)\, \mathrm{d}t \right\} \tag{3a}$$

$$\text{s. t. } \frac{\partial \phi(\mathbf{x}, t)}{\partial t} = -F(\bullet)|\nabla \phi(\mathbf{x}, t)| - \mathbf{v}(\mathbf{x}, t) \cdot \nabla \phi(\mathbf{x}, t) \tag{3b}$$

$$\text{in } (\mathbf{x}, t) \in \Omega \times (0, \infty)$$

$$T(\mathbf{x_f}; F(\bullet)) = \min_t \{t : \phi(\mathbf{x_f}, t) \leq 0\}, \tag{3c}$$

$$\phi(\mathbf{x}, 0) = |\mathbf{x} - \mathbf{x_s}|, \tag{3d}$$

$$p(t) = F(t)^{n_p}, \tag{3e}$$

where $p(t)$ is the power function, $n_p \geq 0$, and other variables are as defined above and listed in Table C.5. For an instance of $F(\bullet)$, the scalar field $\phi(\mathbf{x}, t)$ is a reachability-front-tracking level-set function and the viscosity solution of the level-set Hamilton–Jacobi eq. (3b) with initial conditions (3d) and the subsequent solution to the backtracking Eq. (4),

$$\frac{\mathrm{d}\mathbf{x}^*}{\mathrm{d}t} = -\mathbf{v}(\mathbf{x}^*, t) - F(\bullet)\frac{\nabla \phi(\mathbf{x}^*, t)}{|\nabla \phi(\mathbf{x}^*, t)|}, \quad 0 \leq t \leq T(\mathbf{x_f}; F(\bullet)) \quad \text{and} \quad \mathbf{x}^*(T) = \mathbf{x_f}, \tag{4}$$

yield the continuous-time history of the time–optimal vehicle heading angles, $\theta^*(t)$ (see Lolla et al. (2014c) and Appendix A). An energy-optimal path, Eq. (3a), is thus indeed chosen among time-optimal paths, as Eqs. (3b)–(3e) and Eq. (4) indicate. Next, we provide four remarks.

Remark 1: Effects of variable speeds on energy and time. As $F(\bullet)$ decreases, on the one hand $p(\bullet)$ decreases, but on the other hand, $T(\mathbf{x_f}; F(\bullet))$ increases. The total energy usage E can thus either decrease or increase. Hence, for some arbitrary choice of two $F(t)$ realizations, one can obtain similar optimal arrival times $T(\mathbf{x_f}; F(\bullet))$, but very different energy consumption (and vice–versa). In all cases, the above optimization problem will select the time-optimal path with $F(t)$ corresponding to the lowest energy usage E.

Remark 2: Energy-optimal paths as a subset of time-optimal paths. The opposite effects of changing $F(\bullet)$ on the the power utilized and total time to reach gives rise to a Pareto-front behavior as used in cooperative game theory (LaValle and Hutchinson, 1998). We illustrate such results in Section 6. This behavior provides the freedom to select the energy-optimal path that completes a mission in time-optimal manner for a given time frame. In other words, for every arrival time that corresponds to feasible paths, there is at least one energy-optimal path among the many time-optimal paths (as many as there are realizations of $F(\bullet)$ that lead to feasible paths).

Remark 3: Unique optimal arrival time but multiple energy-optimal paths. Among all time-optimal paths (each with different $F(t)$) that reach the end point at the same time, there can be more than one energy-optimal path. Physically, this simply means that at least two paths that are time-optimal with the same arrival also have the same minimum total energy usage E. Such situations can occur not only with man-made machines as AUVs or cars, but also with animals in nature. Mathematically, this is captured by the viscosity solution of the level-set Hamilton–Jacobi Eq. (3b) which allows for the formation of such singularities or shocks, even from smooth initial conditions, see (Lolla et al., 2014c; Lolla and Lermusiaux, 2016).

Remark 4: Power function p(t). The methodology we develop readily allows energy-based path planning for any type of power consumption dependence with relative vehicle speed, i.e., for any function $p(t)$ of $F(t)$ (3e). For example, one could use: $p(t) \propto F(t)$ for a constant drag-force optimal path, which is often used in control theory to introduce fuel-optimal control (e.g., Athans and Falb, 2007); $p(t) \propto F(t)^2$ for a linear drag; or, $p(t) \propto F(t)^3$ for a quadratic drag. Some vehicle designs could also have power consumption that is proportional to fractional powers of $F(t)$. Finally, power functions that sum terms proportional to acceleration and to various drags (skin drags and induced drag, e.g., Sherman et al. (2001)) can also be directly handled (e.g., Subramani, 2014). However, in the examples provided later, we assume that the total time needed for accelerations (the sum of speed-switching periods) is much smaller than the total time spent at constant speed (sum of the times spent without accelerating). In other words, the vehicle accelerates or decelerates from time to time, but most of the time, it does not accelerate. We can then ignore the acceleration costs and only consider a cost of the form $\int F(t)^{n_p} dt$ with fixed n_p. For ubiquity reasons, we also emphasize the common velocity-square dependence, i.e., $p(t) = F(t)^2$.

3. Methodology

Following control theory, energy-optimal paths could be defined as the solution of a 2-point boundary value problem (Athans and Falb, 2007). However, obtaining these solutions for strong dynamic flows is very challenging. The computations are expensive and hence mostly heuristic approximations are employed requiring problem-specific parameter tuning (see for e.g., Aghababa, 2012; Beylkin, 2008). Another approach to solve the nonlinear optimization problem (3) is a trial and error deterministic optimization. Here, starting from a certain type of $F(t)$ or control (e.g., bang-bang, reduced function space), a refinement process can be used to update the discretized $F(t)$ at one instant and iterate one-change-at-a-time until an optimum for that type of $F(t)$ is reached. Clearly this process can be an inefficient step-by-step search without a guarantee of full optimality. A more efficient approach would be to compute the optimal solutions all at once, at least within a space of functions $F(\bullet)$.

A stochastic optimization approach could directly compute energy-optimal solutions for such a class of $F(\bullet)$ in Eq. (3b) and then iteratively converge to the optimal solution by hierarchically generating new classes from existing ones, as needed. For our problem, the function $F(t)$ then becomes a random variable $F(t; \omega)$. With this external stochastic forcing, Eq. (3b) becomes a stochastic level-set equation. Ideally, if the stochastic PDE can be integrated at once for all events ω, then the whole solution distribution can be obtained directly, which is an advantage when compared to a step-by-step search. Such $F(t; \omega)$ can be sampled from a probabilistic distribution (e.g., uniform distribution) or governed by a stochastic process (e.g., Markov process). Of course, it is only for a comprehensive sampling of the now stochastic function space or distribution $F(\bullet; \omega)$ that the stochastic optimization would yield the optimal solution for that space. If feasible, advantages are that the optimum within the space is found in a single, albeit possibly expensive, stochastic optimization step and that the class of time-optimal solutions are rigorously defined by a stochastic PDE. If the sampling is not complete, the optima obtained so far can be used to hierarchically generate new samples from the existing ones, hence refining the optima until convergence. This hierarchical stochastic optimization is an accelerated heuristic deterministic optimization in the sense that the solution for a distribution $F(\bullet; \omega)$ is obtained at each step, instead for a single new realization. A remaining hurdle is the cost of solving the stochastic PDEs. To address this, our new DO level-set stochastic optimization methodology utilizes the nonlinearities of fluid flows and the confinement of all stochastic reachable sets within a growing narrow-band region, the physical space between the zero level sets of the slowest and fastest realizations of $F(\bullet; \omega)$ (see Section 3.2.3).

In what follows, we first set-up the stochastic optimization for energy-optimal path planning. Next, we develop the new stochastic DO level-set PDEs, providing three variants corresponding to different handling of the non-polynomial nonlinearity in the original PDE. Details of derivations are given in Appendix B. Numerical schemes, computational algorithms, and computational complexity are discussed in Section 4.

3.1. Stochastic level-set optimization approach

Considering the nominal speed $F(t)$ as a random variable belonging to a stochastic class, i.e., $F(t) \to F(t; \omega)$, and a deterministic flow field $\mathbf{v}(\mathbf{x}, t)$, we obtain a stochastic Langevin form of the level-set Eq. (3b):

$$\frac{\partial \phi(\mathbf{x}, t; \omega)}{\partial t} = -F(t; \omega) |\nabla \phi(\mathbf{x}, t; \omega)| - \mathbf{v}(\mathbf{x}, t) \cdot \nabla \phi(\mathbf{x}, t; \omega), \quad (5)$$

where $(\mathbf{x}, t) \in \Omega \times (0, \infty)$ and ω denotes a random event. For $F(t; \omega) \geq 0$, we solve the SPDE (5) until the first time instant t such that $\phi(\mathbf{x_f}, t; \omega) \leq 0$, starting from deterministic initial conditions $\phi(\mathbf{x}, 0; \omega) = |\mathbf{x} - \mathbf{x_s}|$ with boundary condition $\frac{\partial^2 \phi(\mathbf{x}, t; \omega)}{\partial \mathbf{n}^2}|_{\delta\Omega} = 0$, where $\mathbf{n}$ denotes the outward normal to $\partial\Omega$. Such a stochastic simulation yields the distribution of the minimum time-to-reach $T(\mathbf{x_f}; F(\bullet; \omega))$ for an externally forced distribution $F(\bullet; \omega)$.

Next, to allow energy optimization, the distribution of energy utilized is computed from $F(\bullet; \omega)$ and $T(\mathbf{x_f}; F(\bullet; \omega))$ as $E(\omega) = \int_0^{T(\mathbf{x_f}; F(\bullet; \omega))} p(t)\, dt$. As mentioned in Section 2, the function $p(t)$ can assume any power law dependence on $F(t)$. Finally, for any choice of the time-to-reach (a particular time or a range of time), the speed function $F(t; \omega)$ that minimizes the energy cost, $E(\omega)$, can be obtained by a search procedure. As we will show, this optimization is efficient for classes of stochastic functions $F(\bullet; \omega)$ that can be efficiently represented by a reduced basis. Such specifications of reduced bases for the space of vehicle-speed time-series will be discussed in Section 4. The overall approach is summarized by a flowchart in Fig. 2.

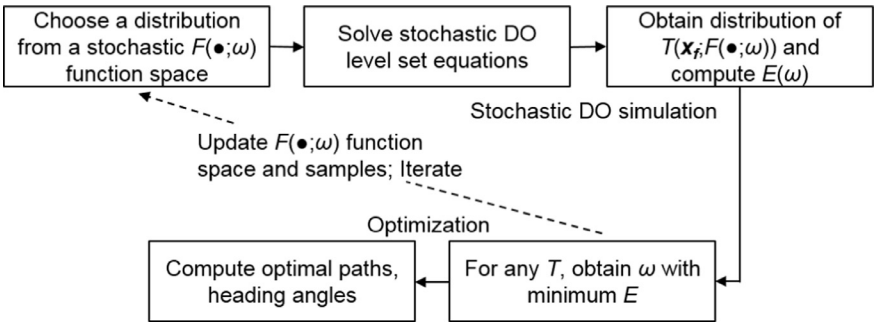

Fig. 2. Flowchart describing the new DO level-set stochastic optimization methodology for computing energy-optimal paths among time-optimal paths for a range of times-to-reach.

We reiterate that the stochasticity comes from the externally forced distribution $F(\bullet;\,\omega)$, and not from the flow field, which for the present work is assumed to be deterministic. However, we note that results can be extended to uncertain flow fields by considering $\mathbf{v}(\mathbf{x},\,t)$ also as a random variable belonging to another stochastic class, i.e., $\mathbf{v}(\mathbf{x},\,t) \rightarrow \mathbf{v}(\mathbf{x},\,t;\,\pi)$, where $\pi \in \Pi$ is a random event representing the uncertainty in the underlying flow field. Such a treatment is illustrated in Lermusiaux et al. (2015), Wei (2015), but only for time-optimal path planning. Energy–optimal path planning under uncertain flows is not considered here.

The most straightforward method to solve the SPDE (5) is through a Monte Carlo (MC) approach. The deterministic level-set PDE (3b) can be solved for different realizations of $F(t;\,\omega)$ to yield a distribution of optimal times $T(\mathbf{x_f};\,F(\bullet;\,\omega))$. Unfortunately, the MC solution is expensive: the computational cost increases with number of realizations used and convergence is slow. Since in (5) $\mathbf{v}(\mathbf{x},\,t)$ is a flow field velocity, an efficient method to solve (5) would exploit the nonlinearities of this flow, which tend to concentrate the responses of the scalar level-set field, ϕ, into specific dynamic patterns. Such a methodology is offered by the DO approach. To the best of our knowledge, this approach had not yet been utilized to determine the stochastic viscosity solution of (5). A numerical challenge in obtaining such DO level-set equations is the presence of the non-polynomial nonlinearity, $\gamma \equiv |\nabla\phi|$. Next, we present ways to handle this challenge and obtain the new DO level-set equations.

3.2. Stochastic DO level-set equations

Before deriving the new stochastic DO level-set PDEs, we first provide the DO decomposition of a general scalar S-PDE and define some notation.

Generic DO equations. Dynamically Orthogonal field equations (Sapsis and Lermusiaux, 2009; 2012; Ueckermann et al., 2013) can be briefly introduced as follows. For a general scalar stochastic continuous field $\phi(\mathbf{x},\,t;\,\omega)$, described by a S-PDE,

$$\frac{\partial\phi(\mathbf{x},t;\omega)}{\partial t} = \mathcal{L}[\phi(\mathbf{x},t;\omega),\mathbf{x},t;\omega], \tag{6}$$

applying a generalized dynamic Karhunen–Loeve (KL) decomposition (a DO decomposition)

$$\phi(\mathbf{x},t;\omega) = \bar{\phi}(\mathbf{x},t) + \sum_{i=0}^{n_{s,\phi}} Y_i(t;\omega)\tilde{\phi}_i(\mathbf{x},t) \tag{7}$$

and an orthogonality condition on the evolution of stochastic subspace

$$\left\langle \frac{\partial\tilde{\phi}_i}{\partial t}, \tilde{\phi}_j \right\rangle = 0 \qquad \forall\ i,j \tag{8}$$

yields the DO equations for the statistical mean $\bar{\phi}$, stochastic coefficients Y_i and deterministic modes $\tilde{\phi}_i$ as

$$\frac{\partial\bar{\phi}(\mathbf{x},t)}{\partial t} = \mathbb{E}[\mathcal{L}]; \tag{9}$$

$$\frac{\partial Y_i(t;\omega)}{\partial t} = \left\langle \mathcal{L} - \mathbb{E}[\mathcal{L}], \tilde{\phi}_i \right\rangle; \tag{10}$$

$$\frac{\partial\tilde{\phi}_i(\mathbf{x},t)}{\partial t} = \sum_{j=1}^{n_{s,\phi}} C_{ij}^{-1}\Gamma_{\tilde{\phi}}^{\perp}\mathbb{E}[Y_j\mathcal{L}], \tag{11}$$

where $\Gamma_{\tilde{\phi}}^{\perp}$ is the operator that returns the component orthogonal to the s-dimensional linear subspace spanned by $\{\tilde{\phi}(\mathbf{x},t)\}_{k=1}^{n_{s,\phi}}$. The original SPDE (6) is recast into the DO equations consisting of a mean PDE (9), the mode PDEs (11), and the stochastic coefficient ODEs (10). The $n_{s,\,\phi}$ modes $\tilde{\phi}_i$ are dynamic, i.e., they form an evolving subspace. The $n_{s,\,\phi}$ stochastic coefficient Y_i are also variable: they evolve the uncertainty within that dynamic subspace. For physical nonlinear systems, the intrinsic nonlinearities in (6) and the corresponding dynamic aspects retained in Eqs. (9)–(11) often enable the truncation to a number of $n_{s,\,\phi}$ modes and coefficients typically much smaller than the dimensions (spatial and stochastic) of the original system. It is these dynamics, and the adaptable size $n_{s,\,\phi}$ (Lermusiaux, 1999; Sapsis and Lermusiaux, 2012), that allow tracking most of the stochasticity of the original variables.

Notation. For every two fields $u(\mathbf{x},\,t;\,\omega)$ and $v(\mathbf{x},t;\omega)$, the spatial inner product is defined as

$$\langle u(\bullet,t;\omega), v(\bullet,t;\omega)\rangle = \int_D u(\mathbf{x},t;\omega)^T v(\mathbf{x},t;\omega)\,\mathrm{d}\mathbf{x}, \tag{12}$$

and the orthogonal component operator is defined as

$$\Gamma_{\tilde{\phi}}^{\perp}G(\mathbf{x}) = G(\mathbf{x}) - \sum_{k=1}^{n_{s,\phi}} \left\langle G(\mathbf{x}), \tilde{\phi}_k \right\rangle \tilde{\phi}_k. \tag{13}$$

The expectation operator is denoted as $\mathbb{E}$. The notation $\bar{\bullet}$ and $\tilde{\bullet}$ refers to means and modes, respectively: $\bar{\phi}(\mathbf{x},t)$, $Y_i(t;\,\omega)$, and $\tilde{\phi}_i(\mathbf{x},t)$ are the mean, ith stochastic coefficients, and ith spatial mode of the spatio-temporal field $\phi(\mathbf{x},\,t;\,\omega)$ while $\bar{F}(t)$, $z(t;\,\omega)$, and $\tilde{F}(t)$ refer to the same but for the temporal scalar $F(t;\,\omega)$. Using the Einstein summation notation, the DO decompositions of $F(t;\,\omega)$ and $\phi(\mathbf{x},\,t;\,\omega)$ are then,

$$F(t;\omega) = \bar{F}(t) + z(t;\omega)\tilde{F}(t), \tag{14}$$

$$\phi(\mathbf{x},t;\omega) = \bar{\phi}(\mathbf{x},t) + Y_i(t;\omega)\tilde{\phi}_i(\mathbf{x},t). \tag{15}$$

We note that the $Y_i(t;\,\omega)$'s and $z(t;\,\omega)$ can represent complex pdf's in accordance with the KL decompositions of $\phi(\mathbf{x},\,t;\,\omega)$ and $F(t;\,\omega)$, respectively. By definition, we also have zero expectations for the coefficients: $\mathbb{E}(z) = 0$ and $\mathbb{E}(Y_i) = 0$. Finally,

the non-polynomial nonlinearity in Eq. (5) is then $\gamma(\mathbf{x},t;\omega) = \left|\nabla(\bar{\phi}(\mathbf{x},t) + Y_i(t;\omega)\tilde{\phi}_i(\mathbf{x},t))\right|$. In the equations to follow, for brevity of notation, $(\mathbf{x}, t; \omega)$ is dropped.

The time-dependent representations equations (14)–(15) of the stochastic process F and ϕ are such that if truncated to a subspace of size $n_{s,F}$ and $n_{s,\phi}$, respectively, each of them capture the most of these processes in the sense of variance (K-L property). Such DO truncations of ϕ are feasible due to the nonlinearities and correlations of environmental flows and, for the case of F, due to the operational constraints on the relative vehicle-speed. The subspace of the stochastic process $F(\bullet, \omega)$ of size $n_{s,F}$ is in the sense of a time-KL decomposition of z. Since F is independent of $\mathbf{x}$, in the sense of its spatial-DO decomposition, the mode $\tilde{F}$ can be set to 1: all F stochastic variations are then represented by the time-KL decomposition of z. When needed to emphasize the subspace reduction of $F(\bullet, \omega)$, we nonetheless denote F as F_{DO}. A list of notation and acronyms we employ is provided in Table C.5 of Appendix C.

Derivations. Inserting the DO decompositions for F (14) and ϕ (15) into the stochastic level-set Eq. (5) along with γ, we obtain the DO expanded level-set equation,

$$\frac{\partial\bar{\phi}}{\partial t} + Y_i\frac{\partial\tilde{\phi}_i}{\partial t} + \tilde{\phi}_i\frac{\mathrm{d}Y_i}{\mathrm{d}t} = -(\bar{F} + z\tilde{F})\gamma - \mathbf{v}\cdot\nabla(\bar{\phi} + Y_i\tilde{\phi}_i) \tag{16}$$

To derive the mean, mode and coefficient equations from (16), special attention is paid to γ. For 2-d in space, $\gamma = \sqrt{\frac{\partial\phi}{\partial x}^2 + \frac{\partial\phi}{\partial y}^2}$, and, for 3-d in space, $\gamma = \sqrt{\frac{\partial\phi}{\partial x}^2 + \frac{\partial\phi}{\partial y}^2 + \frac{\partial\phi}{\partial z}^2}$. We will focus mainly on 2-d in space applications, but the equations to follow are also applicable to 3-d in space. A major challenge is handling this non-polynomial nonlinearities (e.g., Debusschere et al. (2005) and Julier and Uhlmann (1996) for model order reduction based on the polynomial chaos expansion, Lu and Lermusiaux (2016) for biogeochemical reactions). To the best of our knowledge, such attempts have not been made for a γ norm as in (16).

Next, the governing evolution equations for the stochastic DO level-sets are obtained. Details are given in Appendix B and numerical considerations in Section 4. Two approaches for evaluating (or approximating) this γ term are developed. In the first, a separate DO representation is not invoked for γ, but in the second, it is invoked. This second approach further leads to two schemes for evaluating the mean, mode and coefficients of γ. A key difference between these two schemes is their computational costs (see Section 4). Overall, we thus present three DO level-set variants, each originating from (16).

3.2.1. DO–MC Gamma

The first approach we consider is to evaluate γ through a Monte Carlo computation without invoking a separate DO representation for γ. This approach does not fully exploit the redundancy in γ that can be obtained through a stochastic reduced order representation. Nonetheless, it exploits redundancy in ϕ which, as we will illustrate, leads to substantial cost savings. The mean, mode and realization evolution equations for this *DO–MC Gamma* approach are (see Appendix B.1),

$$\frac{\partial\bar{\phi}}{\partial t} = -(\bar{F}\mathbb{E}[\gamma] + \mathbb{E}[z\gamma]\tilde{F}) - \mathbf{v}\cdot\nabla\bar{\phi} \tag{17}$$

$$\frac{\mathrm{d}Y_i}{\mathrm{d}t} = -\left\langle\bar{F}(\gamma - \mathbb{E}[\gamma]) + \tilde{F}(z\gamma - \mathbb{E}[z\gamma]) + Y_k\mathbf{v}\cdot\nabla\tilde{\phi}_k, \tilde{\phi}_i\right\rangle \tag{18}$$

$$\frac{\partial\tilde{\phi}_i}{\partial t} = -C^{-1}_{Y_iY_j}(\bar{F}\mathbb{E}[Y_j\gamma] + \tilde{F}\mathbb{E}[zY_j\gamma]) + \mathbf{v}\cdot\nabla\tilde{\phi}_i - \left\langle -C^{-1}_{Y_iY_j}(\bar{F}\mathbb{E}[Y_j\gamma] + \tilde{F}\mathbb{E}[zY_j\gamma]) + \mathbf{v}\cdot\nabla\tilde{\phi}_i, \tilde{\phi}_n\right\rangle\tilde{\phi}_n. \tag{19}$$

3.2.2. DO–KL Gamma and DO–Taylor Gamma

The second approach we consider introduces a DO representation for γ as

$$\gamma = \bar{\gamma} + \alpha_i\tilde{\gamma}_i \tag{20}$$

where $\bar{\gamma}$, α_i, and $\tilde{\gamma}_i$ are the mean, coefficients and modes, respectively, for the DO representation of γ. The number of modes for representing γ ($n_{s,\gamma}$) and ϕ ($n_{s,\phi}$) in general differ. By inserting (20) into (16), we obtain the mean, coefficient and mode equations as (see Appendix B.2),

$$\frac{\partial\bar{\phi}}{\partial t} = -(\bar{F}\bar{\gamma} + \tilde{F}\mathbb{E}[z\alpha_i]\tilde{\gamma}_i) - \mathbf{v}\cdot\nabla\bar{\phi} \tag{21}$$

$$\frac{\mathrm{d}Y_i}{\mathrm{d}t} = -\left\langle(\bar{F}\alpha_k\tilde{\gamma}_k + \tilde{F}z\bar{\gamma} + (z\alpha_k - \mathbb{E}[z\alpha_k])\tilde{F}\tilde{\gamma}_k + Y_k\mathbf{v}\cdot\nabla\tilde{\phi}_k + z\tilde{F}\tilde{\gamma}, \tilde{\phi}_i\right\rangle \tag{22}$$

$$\frac{\partial\tilde{\phi}_i}{\partial t} = -C^{-1}_{Y_iY_j}(\mathbb{E}[Y_j\alpha_k]\tilde{\gamma}_k\bar{F} + C_{Y_jz}\tilde{F}\bar{\gamma} + \mathbb{E}[Y_jz\alpha_k]\tilde{\gamma}_k\tilde{F}) - \mathbf{v}\cdot\nabla\tilde{\phi}_i - \left\langle -C^{-1}_{Y_iY_j}(\mathbb{E}[Y_j\alpha_k]\tilde{\gamma}_k\bar{F} + C_{Y_jz}\tilde{F}\bar{\gamma} + \mathbb{E}[Y_jz\alpha_k]\tilde{\gamma}_k\tilde{F}) - \mathbf{v}\cdot\nabla\tilde{\phi}_i, \tilde{\phi}_n\right\rangle\tilde{\phi}_n. \tag{23}$$

The challenge of this approach is to obtain an expression for $\bar{\gamma}$, α_i, and $\tilde{\gamma}_i$. We consider two schemes.

DO–KL Gamma: SVD for γ. The mean $\bar{\gamma}$ is obtained as the mean of γ realizations computed from ϕ realizations. The mode and coefficients are obtained by a reduced order SVD of the ensemble spread matrix of γ realizations (see Appendix B.2.1). Dimensionality reduction is achieved by choosing the first $n_{s,\gamma}$ left singular vectors of the ensemble spread matrix as the modes $\tilde{\gamma}_i$ (B.25) and the corresponding first $n_{s,\gamma}$ rows of product of singular values and right singular vectors as the realizations of the coefficients α_i (B.24). Inserting the reduced KL decomposition ($\bar{\gamma}$, α_i, $\tilde{\gamma}_i$) in Eqs. (21)–(23) then completes these equations. The result defines the *DO–KL Gamma* equations.

DO–Taylor Gamma: Taylor series for γ. A DO representation of the non-polynomial nonlinearity can be obtained by applying a Taylor series expansion of γ for the realizations around the dynamic mean $\bar{\phi}$ (see Appendix B.2.2). Truncating such a Taylor series expansion then yields closed expressions for $\bar{\gamma}$, α and $\tilde{\gamma}$, as needed in Eqs. (21)–(23). Specifically, if the first-order Taylor expansion is employed, Eqs. (B.30)–(B.32) define the DO decomposition of γ. Inserting it in Eqs. (21)–(23) then completes these equations. This third variant defines the *DO–Taylor Gamma* equations. This variant is computationally very efficient. However, it works well only when the local stochasticity in γ can be approximated by a first order Taylor expansion around the mean (see Subramani (2014)). Higher order terms can be kept in such expansions when computational cost and accuracy justify it (see Subramani, 2014; Gupta et. al, 2016).

Comparisons of the above three variants and related computational costs are provided in Section 4. Next, we provide the boundary and initial conditions, and then the optimization method, all of which are common to the three variants.

3.2.3. Boundary and initial conditions

Boundary conditions for mean $\bar{\phi}$ and modes $\tilde{\phi}_i$'s. In our applications, the boundary conditions (BCs) for the field $\phi(\mathbf{x}, t; \omega)$ are deterministic and linear. Hence, the BCs for the mean $\bar{\phi}$ are as that of all realizations and the BCs for the modes $\tilde{\phi}_i$ are of the same type but with zero values (Y_i's are scalars and do not have BCs). Specifically, at the open flow boundaries of the computational domain, the BC on the field ϕ consists of setting to zero the second-order

derivative of ϕ in the normal direction. The same BC is thus also used on the mean and modes. This is to ensure that at first order, the expanding level sets can freely advect out of the domain in the sense that they maintain their local slope (curvature at first-order). More complex open BCs for ϕ could be used, e.g., setting a higher-order derivative to zero, but the second order BC has been sufficient for our applications. Obstacles are treated as computational masks (for the mean and modes too), with zero vehicle and zero flow velocities, so as to prevent penetration of level–sets.

Initialization of the DO representation of $\phi(\boldsymbol{x}, t; \omega)$. For any particular realization, the deterministic initialization of $\phi(\mathbf{x}, t; r)$ would be done with a signed distance function from the starting point $\mathbf{x_s}$. A small circle of zero level-set contour is then obtained around the start point by locally subtracting a small number from the $\phi(\mathbf{x}, t; r)$ field. Since all realizations start from the same point $\mathbf{x_s}$, initially i.e. at $t = 0$, all the points away from this initial circle have the same $\phi(\mathbf{x}, t; r)$ for all realizations. After the simulation starts, the zero level-set contour of the fastest $F(t; r)$ realization grows the farthest and that of the slowest $F(t; r)$ grows the least. Moreover, all other realizations have their zero level–set contours confined to the physical space between the slowest and fastest realizations (Lolla and Lermusiaux, 2016; Subramani, 2014). Hence, initially, only a narrow computational band around the initial circle matters. We thus run an ensemble of very short deterministic ϕ simulations for an ensemble $F(t; r)$ and so obtain an ensemble of $\phi(\mathbf{x}, t; r)$ within this computational band. The mean, mode and coefficients of the stochastic DO level-set simulation can then be initialized from this ensemble. The mode and coefficients are obtained by performing a SVD (i.e., KL decomposition) of the mean–removed $\phi(\mathbf{x}, t; r)$ and retaining sufficient left singular vectors as the initial modes. If enough modes are not used initially, as the simulation advances, more modes can be added (Sapsis and Lermusiaux, 2009). Such additions can be seen as re-initialization along the way. In the present examples, the number of modes $n_{s,\phi}$ and $n_{s,\gamma}$ vary between 20 and 100.

3.3. Optimization

The optimization of Eq. (3a) is performed after the above stochastic DO level-set equations (one of the three variants) and backtracking equation are solved, using the DO representation of the stochastic speed $F(\bullet; \omega)$ as external forcing. The solutions of these equations provide the distribution of minimum time-to-reach $T(\mathbf{x_f}; F(\bullet; \omega))$ and distribution of energy utilized $E(\omega)$, each corresponding to the DO representation of $F(\bullet; \omega)$. This information allows searching for the energy-optimal paths for each arrival time frame.

First, recall that for any pre-specified $F(t)$, the solutions of Eqs. (1)–(2) (see Section 2) provide the time-optimal path to reach the target $\mathbf{x_f}$ and thus also the optimal arrival time, among all vehicles operating at relative speed $F(t)$. Second, consider that we are interested in a single arrival time and that the vehicle follows a pre-specified relative speed realization event 1, i.e., $F_1(t) = F(t; r = 1)$. We do not want to operate this vehicle for more than the minimum possible time as any more time will lead to higher energy consumption and any less time would not reach the target. Next, consider another vehicle with pre-specified relative speed realization event 2, i.e., $F_2(t) = F(t; r = 2)$. We also want to operate this vehicle for its optimal time duration. If $F_1(t)$ and $F_2(t)$ have the same optimal arrival time, then the vehicle with the lower energy usage is preferred among the two. If $F_1(t)$ and $F_2(t)$ have different optimal arrival times, they are not compared to each other, but to other realizations that have the same arrival time. Generalizing, consider now a distribution of pre-specified realizations $F(t; \omega)$. If for each arrival time T, we obtain the exhaustive subset of realizations $F_T(t; \omega)$ whose optimum time-to-reach $T(\mathbf{x_f}; F(t; \omega))$ is that arrival time T, we can perform an optimization on the energy usage within this subset, i.e., $E_T(\omega)$, to select the energy optimal realization for that arrival time T. The result is the energy-optimal relative speed $F_T(t)$ and its corresponding path, for that arrival time T. This procedure being repeated for each T, we obtain the energy optimal paths for each arrival time T, among the distribution of time-optimal paths for that T.

Returning to the stochastic DO level-set PDEs, they are forced by the DO representation of $F(\bullet; \omega)$ and, for each of the sample $F_{DO}(t; \omega)$ considered, they predict the optimal time-to-reach the target. Thus, in terms of a reduced-order DO representation of F, the optimization (3a) becomes

$$F^*_{\mathrm{DO}}(t) = \arg\min_{F_{\mathrm{DO}}(\bullet;r)} \int_0^{T(\mathbf{x_f};F_{\mathrm{DO}}(\bullet;r))} p(t;r)dt, \tag{24}$$

where p is the power function (Section 2). In the discrete histogram sense, the stochastic DO level–set optimization thus provides the energy–optimal path(s) for each arrival time frame (small time bin). Discrete algorithms and numerical schemes are discussed next.

Table 1
Stochastic DO Level-Set Optimization: Algorithm.

Stochastic DO level-set simulation

1. Sample $r = 1, \ldots, n_r$ realizations of relative vehicle speeds for duration $T_{\max}$ from a class of stochastic processes and its DO (KL) representation $F_{DO}(\bullet; r)$ (14). Set $T_{\max}$ to be the time required for the slowest relative speed considered to reach the target.
2. Solve the stochastic DO level-set Eqs. (17)–(19), or Eqs. (21)–(23), with n_r realizations and $n_{s,\phi}$ modes to compute the n_r minimum times to reach the target, $T(\mathbf{x_f}; F_{DO}(\bullet; r))$, corresponding to each relative speed realization $F_{DO}(\bullet; r)$.
3. Compute the energy utilization for each realization using $E(r) = \int_0^{T(\mathbf{x_f};F_{DO}(\bullet;r))} p(t; F_{DO}(\bullet; r))dt$.

Optimization

4. For each queried arrival time or time frame (bin), identify all realizations from the stochastic DO level-set simulation that reach the target in the queried time bin.
5. For each of these subsets of realizations, select the realization that utilized the minimum energy and compute its time-optimal path using the backtracking Eq. (4).

Iterate

6. If needed, re-sample the function space $F(\bullet; \omega)$ or expand this function space by (machine) learning

4. Algorithms and numerics

The stochastic optimization algorithm (Table 1) consists of two core successive steps: the stochastic simulation for a given function space of vehicle speeds and the optimization for energy–optimal paths. As introduced in Fig. 2, these core steps can be iterated if the function space of vehicle speeds is re-sampled or improved by (machine) learning. The stochastic simulation is performed by integrating any of the three DO variants (Section 3), depending on cost and accuracy considerations as we will explain shortly. The result is energy-optimal paths among time-optimal paths for a vehicle navigating in a dynamic flow. Critically, what is computed is not the energy-optimal path for a single arrival time but energy-optimal paths for a range of arrival times, all at once.

Next, we discuss how the viscosity solutions (Osher and Sethian, 1988) for an ensemble of deterministic level-set HJ equations can be efficiently captured by the stochastic DO level-set equations. We then showcase numerical schemes and algorithms to handle the stochastic γ term. Finally, we describe the sampling

of the space of relative vehicle speeds, the pruning of *a priori* too energetic speed time-series, the overall computational complexity, and the optimization.

Stochastic DO level-set equations and Monte Carlo in the stochastic subspace. As explained in Section 3.2, the new stochastic DO level-set equations reduce the computational cost by dynamically using the nonlinearities and spectrum properties of ocean flows, and by using a reduced DO representation $F_{DO}(\bullet;\ \omega)$ for the space of relative speed functions. As a result, a large number of integrations of the original deterministic level-set PDE (as would be done in a classic Monte Carlo (MC) solution) is no longer required. Instead, one solves a mean PDE and a few modes PDEs and stochastic coefficient ODEs. For these latter $n_{s,\ \phi}$ stochastic ODEs (which are much cheaper to solve than the original PDE), an efficient DO numerical scheme (Ueckermann et al., 2013) employs a MC solution. This strategy corresponds to time integrating each coefficient on a realization-by-realization basis albeit in the stochastic subspace. This provides major computational savings: the MC computation occurs only in the dynamic subspace and the coefficient equations are ODEs. As a result, for typical ocean problems, the computational time required for the MC computation is 2–4 orders of magnitude smaller than the original MC computation in the full stochastic space, for the same number of realizations n_r. We note that this is a novel application of the DO method (previously used for uncertainty quantification): for the first time, it is employed as a dynamic model-order reduction scheme to perform stochastic PDE simulations for an optimization scheme.

Numerical schemes for the stochastic DO level-set equations. The DO level-set equations are solved using a finite volume framework (Ueckermann and Lermusiaux, 2011). A forward Euler time stepping scheme is used to integrate the mean, modes and coefficients of ϕ in time. The advection terms are computed using a Total Variation Diminishing scheme. The non-polynomial nonlinear term, $\gamma = |\nabla\phi|$ is computed using an upwind scheme, i.e., Sethian's viscosity solution (Osher and Sethian, 1988). For the *DO–MC Gamma* and *DO–KL Gamma* variants in Section 3.2, γ is computed for each realization and their individual upwind characteristics are used. For the *DO–Taylor Gamma* variant, the upwind direction for all the modes are taken to be the upwind direction for the mean. For more on numerics for Eqs. (17)–(19) and Eqs. (21)–(23), we refer to Subramani (2014).

Handling the non-polynomial nonlinearity γ. The three DO variants, i.e., *DO–MC Gamma*, *DO–KL Gamma*, and *DO–Taylor Gamma* in Section 3.2, provide a different computational estimate of the γ term or of its DO representation (its mean, mode and coefficient). These different algorithms are now compared. In the *DO–MC Gamma* variant, the DO representation for γ is not used. Instead, a realization of γ is computed for each of the n_r realizations of ϕ and $F_{DO}(\bullet;\ r)$, and evolve according to Eqs. (17)–(19) themselves.

In the *DO–KL Gamma* variant or SVD for γ (Section 3.2.2), the $n_{s,\ \gamma}$ modes are estimated by a reduced order SVD (as a reminder, $n_{s,\ \gamma}$ can be different from $n_{s,\ \phi}$). It is desirable that these modes $\tilde{\gamma}_i$ are computed at every time step. However, to compute such a SVD, the cost is $O(n_r n_g^2)$. A Lanczos method or a Krylov subspace method can reduce the computational effort to $O(n_r n_{s,\gamma}^2)$ (Gugercin, 2005). Nonetheless, at each time step, such SVDs can become computationally expensive for large problems. In some cases, the DO subspaces can change less quickly than the coefficients within the subspace. Hence, for sufficiently smooth environmental flow fields and vehicle speed functions, an approximation for the γ modes dynamics consists of updating $\tilde{\gamma}_i$ only intermittently, e.g., every few time steps. We refer to such an algorithm which updates $\tilde{\gamma}_i$ only every p time-steps as the *p-delay-SVD DO–KL Gamma*. Such intermittent SVD computations can save computations but still solve the DO equations to within acceptable error levels. Of course, the modes $\tilde{\phi}_i$ for ϕ are still updated at each time-step using Eqs. (21)–(23).

For the *DO–Taylor Gamma* variant, the mean, mode and coefficients for γ are approximated by a first-order Taylor expansion. This approximation gives good results as long as the pdf of the γ function is well approximated by a locally linear representation. Since the pdf of γ depends on the pdf of the level-sets governed by the sample path Eq. (5) and on the pdf of the gradient of level-set realizations, this approximation can be good but not in all cases. This result is illustrated in Section 5.

Higher-order terms in the Taylor expansions can be kept when computational cost and accuracy justify it; for example, second order schemes are used in Subramani, 2014; Gupta et al., 2016. However, local Taylor series have a computational cost that increases with $n_{s,\ \gamma}$ to a power that depends on the order. Hence, they can become more expensive than the *DO–KL Gamma* and *DO–MC Gamma* methods. This also remains true for local polynomial approximations of the nonlinear γ function (Gupta et al., 2016).

Duration of the stochastic simulation. The stochastic simulation is executed for a time duration that is just greater than the time required for the slowest vehicle, i.e., the vehicle having a constant instantaneous speed equal to the minimum allowed speed, to reach the target. Any other time-series of vehicle speed specification will reach the target before the slowest vehicle.

Relative speed function space and its stochastic sampling. The sampling of $F(\bullet;\ \omega)$ that generates relative speed realizations $F(t;\ r)$ is a key step of our algorithm. In our treatment, the stochasticity in the level-set equation (5) arises from this externally forced $F(\bullet;\ \omega)$. Among the realizations $F(t;\ r)$, we search for those that lead to the minimum energy paths. An exhaustive discretized sample class can be built by directly sampling the complete combinatorial space formed by discretized speed and discretized time. However, the sample size of this direct sampling grows exponentially (Lin and Fisher, 2012) with speed range and time duration. Obtaining such a sample is NP-complete (Gomes et al., 2006). Markov-chain-based sampling is usually used in applications where such combinatorial sampling is required (Lin and Fisher, 2012).

For our path planning in environmental flows, the inherent time and space scales can be used to reduce the size of the space of relative speed time-series. Operational constraints on vehicle operations also further reduce this search space. For example, in our coastal ocean applications, typical time and space dynamical scales are hours to days, and O(1 km to 100 km), respectively. Typical operational constraints are limits on the frequency of accelerations and preferred operation at constant relative speeds, e.g., constant for one or more hours (Ramp et al., 2009; Haley et al., 2009; Leonard et al., 2010). Hence, a first reduced relative speed space we consider are Markov processes (Gelb, 1974) such as an exponentially-decorrelated-in-time random process. A second computationally tractable option is a switch-sampling algorithm where the frequency of possible speed switches is set by the environmental scales and operational constraints. These and other options are discussed in (Subramani, 2014).

Here, we will focus on the switch-sampling algorithm. It is a randomized approximation of the exhaustive direct sampling. In direct sampling of a combinatorial space, for l levels of discretized speed and $n_{sw,F}$ discrete times, the total sample size is $l^{n_{sw,F}}$. For example, if we have 2 levels of discretized speed, 5 cm/s and 25 cm/s, and we divide a total duration of 2 h into two discrete time intervals of 1 h each, then the combinatorial space consists of 4 samples, viz., (5,5), (5,10), (10,5), (10,10) where (a, b) refers to a vehicle speed specification of a cm/s for 0–1 h, and b cm/s for

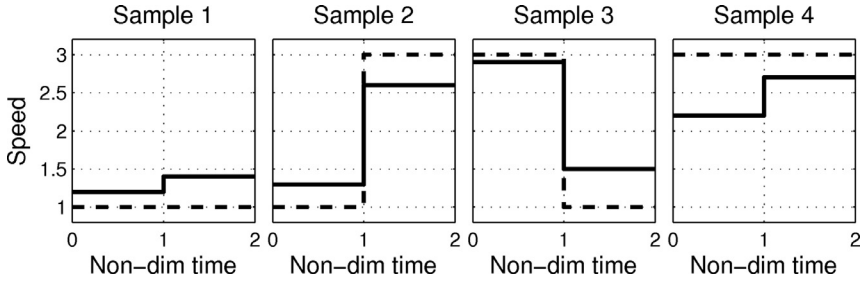

Fig. 3. Dotted lines represent the exhaustive sample with 2 speeds and 2 time intervals (or 1 switch). The solid lines represent the sample obtained by switch sampling which divides the entire speed range in two and for each time interval chooses a random value within one of the two ranges.

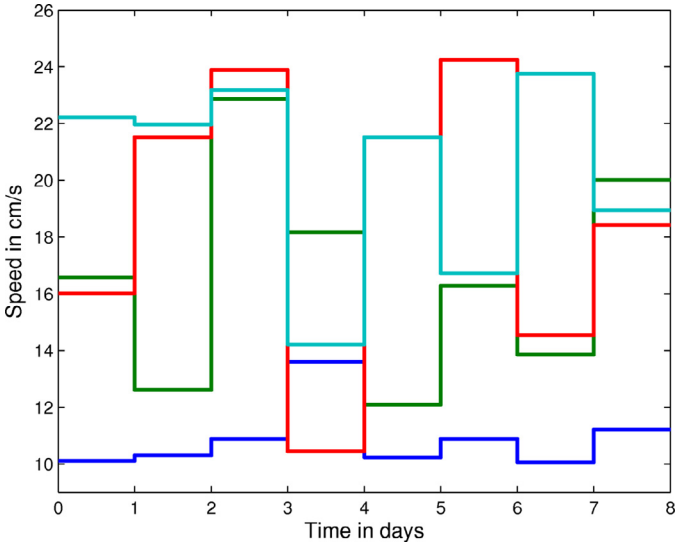

Fig. 4. Some realizations chosen from a sample obtained with a switch–sampling scheme. Here, we switch the samples every day over a 8 days period, and 4 speed levels are considered. The represented samples are instances from a sample space with $4^8 = 65,536$ samples.

1–2 h. We could randomize a and b and divide the range between 5 and 25 cm/s into $l = 2$ such that $5 < a < 15$ and $15 < b < 25$. Now the 4 samples will be (a,a), (a,b), (b,a), (b,b) where a and b are random numbers in their corresponding range. In this case, we say that the vehicle *switched* its instantaneous speed after 1 hr and then maintained the new speed for next 1 h. This is exemplified in Fig. 3. In general, we will fix the maximum number of switches in nominal speed that the vehicle can make during the entire mission. Such a more complex situation is shown in Fig. 4.

The approximation of the switch-sampling is the coarser resolution in both discrete speeds and switching times than in direct sampling. The randomization within this coarser resolution aims to remedy for this: the structured and relatively strong environmental flows are such that ranges of speeds lead to very similar behavior and do not need to be sampled with refined grids. As we will see, another advantage of switch–sampling is that using random numbers in ranges, a structured approach is taken to sample the large combinatorial space, and with enough samples, the method can find the energy optimal paths.

Pruning. When compared to a constant (single) speed vehicle, our goal is to find the path with a variable vehicle speed that saves the most energy while still arriving at the same time or earlier. Hence, if any realization in the stochastic DO simulation spends more energy than a constant relative speed vehicle, then it is not of interest. As such, our algorithm initially computes optimal paths and arrival times for all constant relative speeds. This information is then utilized to prune realizations with variable $F_{DO}(t;\, r)$ that would for sure consume more energy: i.e., for the same arrival time than these optimal constant relative speed paths, all of the realizations $F_{DO}(t;\, r)$ that have an energy usage $E(r)$ that is as large as that of the corresponding time–optimal constant relative speed can be eliminated. This removal of too energetic realizations $F_{DO}(t;\, r)$ is done before the start of the stochastic DO level–set computation, which leads to significant savings.

Overall stochastic computational complexity. Per time-step, the computational costs of the different stochastic solvers are as follows. The direct Monte Carlo solution has a computational cost that scales as $O(\beta n_r n_g)$, where $\beta \sim O(10\text{–}100)$ for typical advection schemes utilized (e.g., Total Variation Diminishing, Ueckermann and Lermusiaux (2011)). The *DO–MC Gamma* variant has a cost that scales as $O(n_r n_g) + O(n_r n_{s,\phi}^2)$ for γ and DO advection respectively. The *DO–KL Gamma* and *DO–Taylor Gamma* variants reduce the overall computational cost to $O(n_r n_{s,\phi}^2)$. Note that the *DO–KL Gamma* has an additional cost of computing the SVD of γ realizations which is also $O(n_r n_{s,\gamma}^2)$ when an efficient SVD algorithm is utilized. With pruning, n_r reduces in later time steps thereby reducing costs. For typical coastal ocean applications that we are interested in, $n_{s,\phi} \ll \sqrt{\beta n_g}$. Hence, all DO variants are much cheaper than direct Monte Carlo and provide 100–10,000 times speed up (see also Section 5.1).

Optimization, iteration and learning of vehicle speed functions. A search algorithm is used to find vehicle speed realizations that minimize energy according to Eq. (24). From the stochastic DO level–set simulation (steps 1–3 in Table 1), we obtain an energy-time-vehicle-speed discrete distribution. For a queried arrival time or time frame, we first form a conditional distribution of energy-vehicle-speed by selecting only those discrete samples that reach in the queried time or time frame. The discrete conditional distribution is then sorted according to energy by Quick Sort (Hoare, 1962) and the minima is identified. Alternatively, in applications where the interest is only the absolute minimum energy used, a single loop comparison can be employed to find the realization with the smallest energy utilization. After identifying the discrete vehicle speed realization that results in minimum energy usage for the queried arrival time or time frame, we compute the energy-optimal path using the backtracking Eq. (4). The path thus obtained is energy-optimal among time-optimal paths. In practice, this procedure is completed in parallel for a range of queried times.

If needed, one can iterate and re-sample the function space $F(\bullet;\, \omega)$. For example, for the double-gyre flow in Section 6.2, we tested different sampling algorithms (see above) by changing the correlation-in-time for the Markov process and the duration between switches for the switch-sampling algorithm. Similar iterations were performed in real ocean applications (Subramani et al., 2016). In some cases, one could also expand this function space

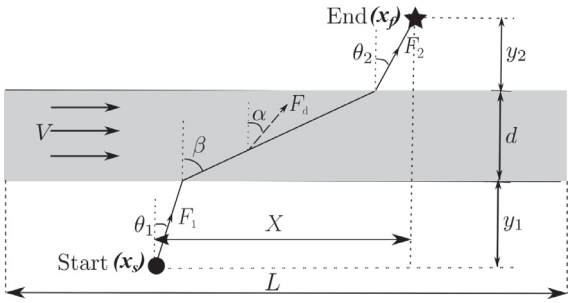

b

$X = 60$	$V = 20$
$y_1 = 20$	$F_{\min} = 10$
$d = 20$	$F_{\max} = 30$
$y_2 = 20$	$L = 100$
	$T = 150$

Case 1 (along the flow)	Case 2 (against the flow)
$\mathbf{x_s} = (20,20)$	$\mathbf{x_s} = (80,20)$
$\mathbf{x_f} = (80,80)$	$\mathbf{x_f} = (20,80)$

Fig. 5. (a) Energy-optimal crossing of a canonical uniform steady front. The shaded region consists of a uniform and steady jet of speed V from west to east. The geometric parameters are: start point, $\mathbf{x_s}$ (circle); end point, $\mathbf{x_f}$ (star); horizontal distance between them, X; vertical distance from start to the front, y_1; width of the front, d; and, vertical distance from the front to the end point, y_2. The nominal vehicle speed parameters are: speed from the start point to the front, F_1; in the front proper, F_d; and, from the front to the end point, F_2. The headings are marked with arrows. The numerical domain is a square of side L with the steady uniform zonal front in the middle. (b) Fixed parameter values (non-dim.)

Table 2
The values of the numerical parameters employed for the MC and DO solutions of the S-PDEs, used to validate the DO solutions. The physical parameters are in Fig. 5b.

	n_r	$n_{s,\phi}$	$n_{s,F}$	$n_{s,\gamma}$	$n_{sw,F}$	l	dx	dy	dt
Direct MC	4096	–	–	–	6	4	3.33	3.33	1
DO–MC Gamma	4096	20	1	–	6	4	3.33	3.33	1
DO–KL Gamma	4096	20	1	20	6	4	3.33	3.33	1
DO–Taylor Gamma	4096	20	1	20	6	4	3.33	3.33	1

by (machine) learning (e.g., MacKay, 2003; Murphy, 2012; Lu and Lermusiaux, 2016).

5. Validation

We perform a two step validation. First, we answer the question on whether the new stochastic DO level-set equations, (17)–(19) or (21)–(23), solve the original SPDE (5) accurately. We introduce a canonical test case and compare the DO solution with that of the MC method. We show that the DO method is much cheaper and is indeed capable of reproducing any of the MC solutions with less than 2% error for 99.5% of the realizations. Second, we employ a benchmark to test if our stochastic DO level-set optimization computes accurate energy optimal paths. Specifically, we develop a semi-analytical energy-time nested nonlinear double-optimization for a simple test case. Results show that the stochastic optimization agrees with this independent semi-analytical solution, with the additional advantage that it solves the optimization for many arrival times at once, whereas the latter only provides a solution for a single arrival time.

The canonical test case consists of determining energy-optimal paths for the crossing of a simple idealized front, as illustrated in Fig. 5a. The environmental flow is a uniform and steady jet, flowing from west to east in a rectangular domain. The mission is for a vehicle to start from a point in the south west region of the domain and travel to a point in the north west region while minimizing the energy usage for a given arrival time. The values of the physical parameters are provided in Fig. 5b.

5.1. Stochastic level-set PDE solution validation

In this section we compare the DO method solution with the MC method solution. We use the stochastic DO level-set equations to track the zero level-set contour for all realizations at once. The MC solution tracks the evolution of the zero level-set by solving the deterministic level–set equation for all realizations separately. The MC solution is thus considered as the ground truth which the DO solution attempts to compute, utilizing dynamical redundancy for a drastic increase in computational efficiency. Hence, comparing the two solutions provides a validation for the DO method.

The Frechet distance (Alt and Godau, 1995), which measures the maximum distance between two closed curves, is used as the metric for comparing two zero level-set contours. We measure the discrete Frechet distance, which takes into account the location and ordering of points (Danziger, 2011), as a fraction of the grid spacing. This quantifies the relative measure of closeness of zero level-set contours.

The three DO variants are each compared with the MC method. The numerical parameters, provided in Table 2, are chosen such that the direct MC solution completes all realizations within reasonable runtime.

The results are illustrated in Fig. 6. Each column first shows zero level–sets for a randomly chosen realization for 3 time instances, comparing the solution of each DO variant with that of the MC method. The first three rows are the time instances. The fourth row shows how the distance metric (the ratio of the Frechet distance to grid spacing) varies with arrival time. We find that the zero level-sets are different by a Frechet distance of the order of grid spacing or smaller. The numerical stochastic DO level-set solutions thus introduce an error of about 1% of the domain size (which is less than the spatial discretization used here).

Ultimately, we are interested in computing optimal arrival times for all realizations. Hence, we compare the arrival times computed by the three DO variants and MC in Fig. 6c, again without pruning so as to compare all realizations. We find that for 4096 realizations, all samples have less than 4% relative error, i.e., the error in DO arrival time as a fraction of the MC arrival time, for both the *DO–MC Gamma* and *DO–KL Gamma* variants, with more than 99.5% of the samples having less than 2% relative error. For *DO–Taylor Gamma*, the error is slightly larger but still all samples have less than 6% relative error and 95% of the realizations have less than 2% relative error. This higher error for *DO–Taylor Gamma* is expected as it assumes that a first–order Taylor approximation is sufficient while the other two variants do not.

For the present test case (Fig. 5a, b, Table 2), the CPU time requirement on a single CPU with 4 cores for direct MC is

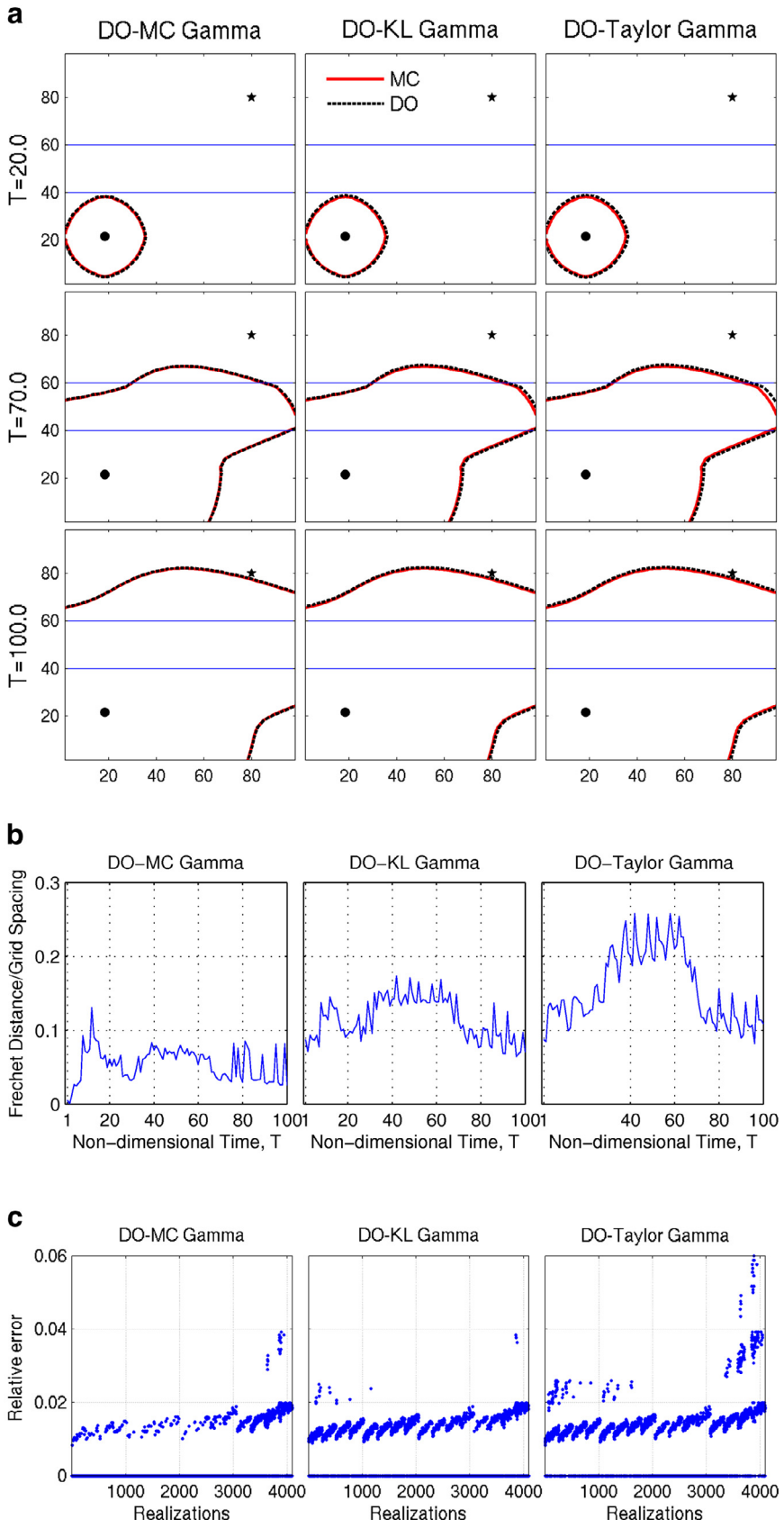

Fig. 6. (a) First column compares *DO–MC Gamma* with MC; second column, *DO–KL Gamma* with MC; and, third column, *DO–Taylor Gamma* with MC. Each row corresponds to separate time instances in increasing order. (b) Ratio of Frechet distance between the zero level–set contour computed by the three DO and MC estimates. This distance metric measures the maximum distances between the zero level-set contours. Results indicates that the error between the three DO and MC solutions are $O(\Delta x)$ or better. (c) Relative error in time-to-reach for all realizations simulated, again for the three DO variants. The time requirement on a CPU with 4 cores for direct MC is approximately 6000 s. However, for the DO methods, it ranges from 100 s (*DO–MC Gamma*) down to only 10 s (*DO–KL Gamma, DO–Taylor Gamma*).

approximately 6000 s. However, the time requirement for the DO methods range from 100 s (*DO–MC Gamma*) up to 10 s (*DO–KL Gamma, DO–Taylor Gamma*).

5.2. Methodology validation

The canonical flow permits a semi-analytical solution for computing the path that minimizes energy among time optimal paths but for a single specific arrival time at a time (Subramani et al., 2015). Here, we develop this semi-analytical solution and use it to validate the stochastic DO level-set optimization.

For the semi-analytical solution, we first consider the motion of the vehicle from the start point to the uniform steady front. Since there is no flow affecting the vehicles motion in this part of the path, the total displacement of the vehicle depends only on its nominal speed and a straight line path would minimize the travel time. Moreover, the energy consumed by the vehicle which varies as a power function of $F(t)$ (see Section 3), would be minimized if a single mean speed is used instead of a variable speed. This fact follows from an application of Hölder's inequality to the power function,

$$\int_T F(t)\mathrm{d}t \leq \left[\int_T F(t)^{n_p}\mathrm{d}t\right]^{\frac{1}{n_p}}\left[\int_T \mathrm{d}t\right]^{1-\frac{1}{n_p}} \tag{25}$$

$$\int_T \left(\frac{\int_T F(t)\mathrm{d}t}{\int_T \mathrm{d}t}\right)^{n_p}\mathrm{d}t \leq \int_T F(t)^{n_p}\mathrm{d}t, \tag{26}$$

showing that navigating with a time averaged speed consumes less energy than navigating with a variable speed.

Next we consider the motion of the vehicle within the *uniform* and *steady* front proper. As the flow is from west to east along the x–direction, it only affects the vehicle's motion in that direction. To cross the uniform steady flow, the vehicle should thus use a single speed to minimize energy consumption, because of similar Hölder's inequality arguments than for the motion prior to reaching the front. After exiting the front, the analysis is similar to before entering the front. Therefore, for a given travel time, the energy optimal path is executed by a vehicle that moves at a constant speed from the start point to the steady front at some to-be-determined point, then another speed (same or different) for the time optimal motion within the uniform steady front, and finally another speed from the steady front to the target. These arguments allow us to setup our double-optimization problem, 'energy–optimality subject to time-optimality'.

Combining the above, we set the time-variation of the unknown optimal relative speed to be the uniform speeds F_1, F_d, and F_2, from start to the steady front, within the steady front, and from the exit of the steady front to the end point, respectively. Let $\mathbf{U}$ denote the *total* effective velocity of the vehicle in the flow, as seen by a ground observer. Within the steady front, the component of $\mathbf{U}$ in the x–direction is $U_x = F_d \sin\alpha + V$ and in the y–direction, $U_y = F_d \cos\alpha$. The direction of resultant velocity and heading angle are related through the relation, $\tan\beta = \frac{U_x}{U_y} = \tan\alpha + \frac{V}{F_d}\sec\alpha$. Outside the steady front, the relations are the same, but with $V = 0$. Now, let X be the total downstream displacement of the vehicle, i.e. in the x direction. We have, from trigonometry, $X = y_1\tan\theta_1 + d\tan\beta + y_2\tan\theta_2$. Finally, the total travel time T can be written as the sum of travel times in each individual region, $T = \frac{y_1}{F_1\cos\theta_1} + \frac{d}{F_d\cos\alpha} + \frac{y_2}{F_2\cos\theta_2}$. We want to determine the energy optimal path, for each arrival time such that they are also time-optimal. Hence, assuming for now, a general energy cost over $\mathrm{d}t$, $\mathrm{d}E = p(t)\,\mathrm{d}t = F(t)^{n_p}\,\mathrm{d}t$ where $n \geq 1$, we obtain the total energy expended from the start point to the end point as: $E = F_1^{n_p-1}\frac{y_1}{\cos\theta_1} + F_d^{n_p-1}\frac{d}{\cos\alpha} + F_2^{n_p-1}\frac{y_2}{\cos\theta_2}$. All together, for a fixed time-to-reach the target, the double-optimization problem is thus,

Table 3
Parameters of the energy optimal path that reaches the end point at time $T = 55$. The two results are within PDE-discretization errors.

Parameter	Using dual optimization	Using stochastic DO level-set optimization
θ_1	29°	28°
θ_2	29°	23°
α	34°	40°
β	61°	65°
F_1	28.2	29
F_d	21	22.4
F_2	28.2	26.8

$$\min_{F_1,F_d,F_2} E = F_1^{n_p-1}\frac{y_1}{\cos\theta_1} + F_d^{n_p-1}\frac{d}{\cos\alpha} + F_2^{n_p-1}\frac{y_2}{\cos\theta_2} \tag{27}$$

$$\text{s.t.} \qquad X = y_1\tan\theta_1 + d\left(\tan\alpha + \frac{V}{F_d}\sec\alpha\right) + y_2\tan\theta_2 \tag{28}$$

$$T = \min_{\theta_1,\alpha,\theta_2} \frac{y_1}{F_1\cos\theta_1} + \frac{d}{F_d\cos\alpha} + \frac{y_2}{F_2\cos\theta_2} \tag{29}$$

$$\theta_1, \theta_2, \alpha \geq 0, \quad F_{\min} \leq F_1, F_d, F_2 \leq F_{\max}, \quad n_p \geq 1 \tag{30}$$

where X, T, $F_{\min}$, and $F_{\max}$ are inputs to the optimization problem. The time constraint for the outer energy optimization is another inner time optimization: indeed, F_1, F_d, F_2 are the unknowns optimized within the outer energy loop while θ_1, α, θ_2 are the unknowns optimized within the inner time loop, given speed value realizations for F_1, F_d, F_2. This completes the derivation of the double minimization problem. Its solution is the energy-optimal path as defined in Section 2, but again, only for a fixed single arrival time.

We note that this *semi-analytical* solution is not straightforward to compute and we employ MATLAB's `fminunc` in a global solve mode to obtain a solution that satisfies the constraints. We terminate the local solves when the step size of variables is below a threshold (set to machine precision). For the physical parameters provided in Fig. 5b (Case 1), and fixing the single target arrival time T to be $T = 55$, we obtain the numerical solution of our double-optimization problem as given in column 1 of Table 3.

Now, we compare this *semi-analytical* solution to that of the stochastic DO level-set optimization. We select samples from the switch-sampling procedure and build a set of 65,536 realizations. The maximum run time, $T_{\max}$, of the stochastic DO simulation is set to the time required by the slowest vehicle to reach as all vehicles faster than this vehicle would reach before $T_{\max}$. The result of this DO optimization with the same parameters as above is given in column 2 of Table 3. The errors between the paths obtained by nonlinear optimization and stochastic DO level-set optimization are of the order of the time and space resolutions. Hence, we only show the optimal path obtained by the latter in Fig. 8a of Section 6. Critically, we note that our stochastic solution provides answers for a wide range of arrival times in addition to the single fixed time T considered here by the *semi-analytical* solution as illustrated next.

6. Applications

6.1. Energy-optimal path planning in a uniform steady front

In Section 5, we presented results only for a particular time to reach. Here, we illustrate all results, demonstrating the full capability of the new methodology, i.e., the ability to compute energy-optimal vehicle speed and path specifications for a range of arrival times, all at once. Two vehicle missions are now considered: the

Table 4
The numerical parameters employed for the stochastic DO simulation of the uniform steady front crossing problem. The physical parameters are in Fig. 5b.

	n_r	$n_{s,\phi}$	$n_{s,F}$	$n_{s,\gamma}$	$n_{sw,F}$	l	dx	dy	dt
Case 1 (along the flow)	65536	100	1	100	8	4	1	1	0.25
Case 2 (against the flow)	65536	100	1	100	8	4	1	1	0.25

first is as that used in Section 5, the second consists of crossing the front against the jet flow.

Crossing the uniform and steady front-downstream. This mission is as in Section 5.2, with physical parameters defined in Fig. 5b (case 1) and illustrated on Fig. 5a. The numerical parameters of the switch-sampling and DO level-set simulations are in Table 4. For each of the $n_r = 65,536$ speed realizations $F(t; r)$ (step 1 in Table 1), the DO simulation computes the optimal time to reach the target (step 2 in Table 1). With these optimal times, the energy utilized by each realization is computed (step 3 in Table 1). Fig. 7 shows the resulting distribution of time to reach and energy utilized, for all samples $F(t; r)$ as dark gray and light gray dots. Each dot corresponds to a different realization. The constant speed samples $F(r)$ are colored according to their respective vehicle speeds. The energy consumption is normalized by the energy requirement of the fastest constant speed vehicle, which is the global time optimal path and is the sample that utilizes maximum energy. We are interested in the vehicle path and speed specifications that require at most the energy usage of vehicles with a constant speed. Hence we rank paths by the percentage of energy saved with respect to a constant speed path with the same arrival time. The dark gray points are realizations that consume less energy than constant speed realizations and lighter gray points are realizations that consume more energy than constant speed realizations. Recall that all constant speed paths are also time optimal. Ranking is thus based on strict energy-optimality.

We first note that the DO stochastic simulation is agnostic and can consider samples $F(t; r)$ that utilize more energy than constant speed samples. However, using pruning described in Section 4, we increase efficiency. A pruned stochastic DO simulation would have discarded and thus not used the light grey colored dots shown in Fig. 7, hence reducing computational cost without changing accuracy. We only show the unpruned version to illustrate the inner working and nuances of the method. From the distribution of energy utilized and time to reach, we can then select *any particular* time to reach (e.g., $T = 55$) or time bin (e.g., $55 \leq T \leq 65$) and isolate the subset of time-optimal paths for that queried time

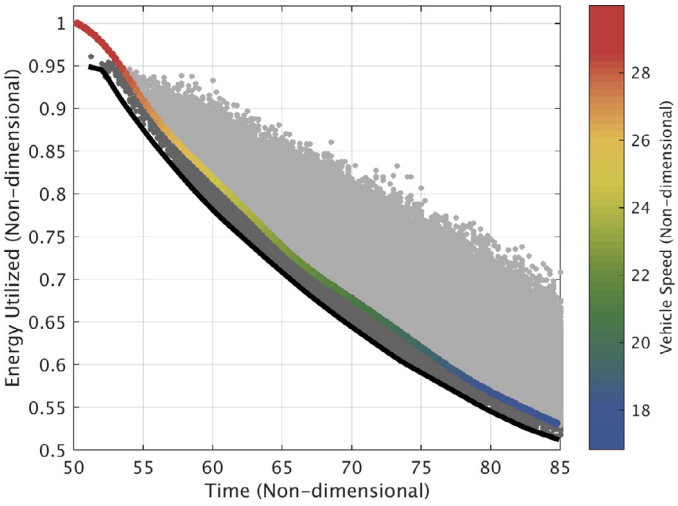

Fig. 7. *Crossing the front-downstream:* Distribution of time to reach (right) and energy utilized (left), for all 65,536 realizations $F(t; r)$, as computed by the stochastic DO level-set optimization. Each dot corresponds to a realization: dark/light gray dots consume less/more energy than the constant speed realizations (dots colored with $F(r)$). These colored dots form the curve of energy-utilization versus time-to-reach for constant speed vehicles. The black line is the energy-optimal versus time-to-reach curve obtained using our methodology, showing its capability of finding energy-optimal speed functions for a range of arrival times.

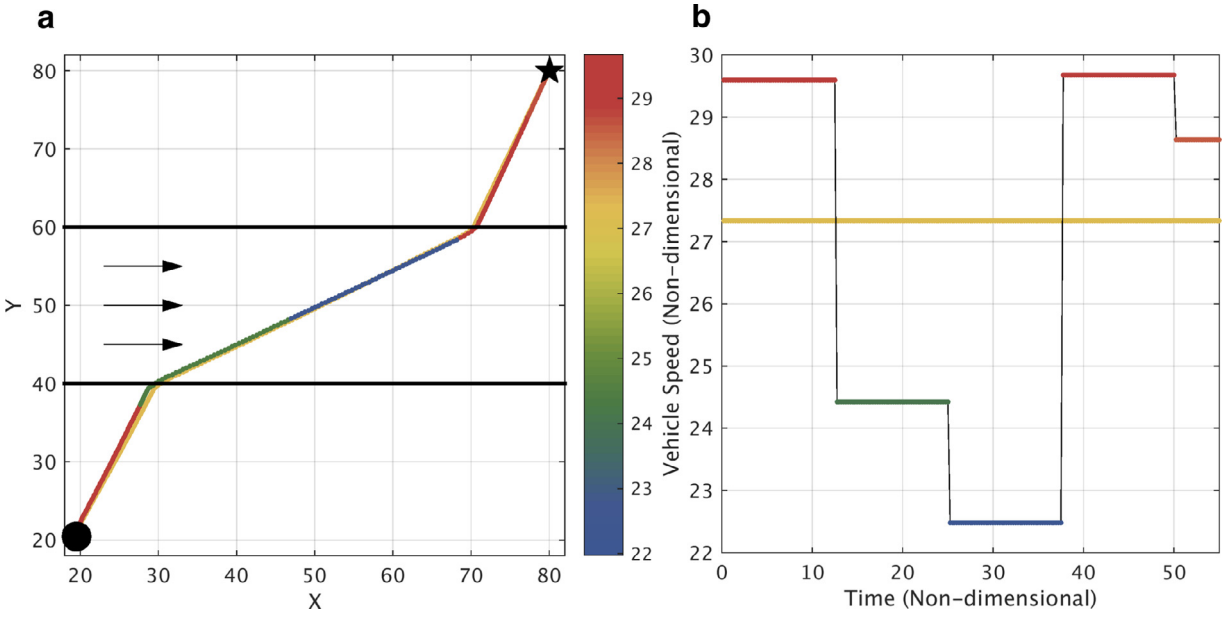

Fig. 8. *Crossing the front-downstream:* (a) Physical paths followed by a constant speed vehicle and by the energy optimal vehicle, for the same arrival time $T = 55$. Both are also time optimal paths for their respective speeds. (b) These instantaneous vehicle speed functions $F(t; r)$, for each of the two vehicles.

(step 4 in Table 1). Finally, we search for the vehicle speed specification $F^*_{DO}(t)$ that optimizes energy consumption among this subset (step 5 in Table 1). These optimizations can be done all at once, for all arrival times. Here, we illustrate only $T = 55$ and thus find the realization with minimum energy for that arrival time T. Other T choices are shown in Subramani (2014) (not shown here). The optimal physical path for $T = 55$ is plotted in Fig. 8a, overlaid with instantaneous vehicle speeds. It consumes only 95% of the energy used by the corresponding constant speed path, also shown in Fig. 8a. Here, the paths are close physically, but the energy optimal vehicle switches to a lower speed within the uniform steady front and utilizes a higher speed outside, as shown in Fig. 8b. The lower speed in the *highway* is an intelligent utilization of the flow to optimize energy consumption.

Crossing the uniform and steady front – upstream. In the second mission (case 2 in Fig. 5b and Table 4), the vehicle has to travel against the flow. Fig. 9 shows its resulting energy-time distribution. First we find that, for the same flow strength as in the first mission, the second mission requires longer travel times for constant speed vehicles. Here, the vehicle has to travel against the flow which delays it. Note that we again show in Fig. 9 the unpruned version of the DO level-set simulations, as in Fig. 7. Next, to illustrate the optimization results, we choose $T = 110$ and compare the energy optimal path for that queried time to a constant speed path with the same arrival time (again, any arrival time T could have been chosen, our method computes energy-optimal paths for each T, e.g., see Section 6.2 for examples). Fig. 10a compares these two paths on the physical domain overlaid by their instantaneous speed. In contrast to case 1, we find here that paths are much more different in the front proper. Nonetheless, the two vehicles (constant speed and energy optimal at variable speeds) have the same arrival time. The energy optimal vehicle utilizes 7% less energy than the constant speed one. When the flow is adverse to the general direction of motion, the energy optimal vehicle employs a higher speed in the front proper and lower speeds outside, so as to reduce the overall energy consumption.

Discussion. If the target is directly (geographically) up North of the start point and both points are symmetric with respect to the uniform and steady jet flow from West to East, the situation is in between the two scenarios described above. The energy-optimal path (not shown) is then a symmetric S shape: the vehicle travels northwestward before reaching the flow, then is advected downstream overshooting the target (to the East), and finally travels northwestward again after exiting the flow to reach the target. In the absence of a flow, the fastest path is a straight line from start to target; it is the flow that makes the vehicle adjust its path to minimize time and energy. In general, seeking optimal paths is nontrivial.

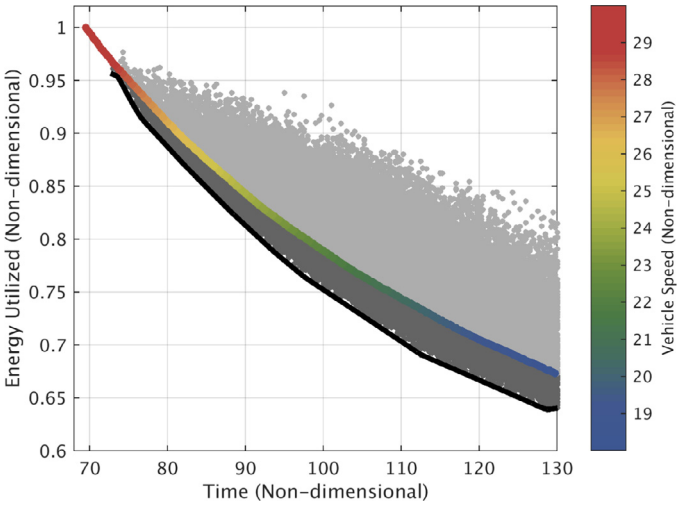

Fig. 9. *Crossing the front-upstream:* as Fig. 7, but for the second mission against the flow. Again, the stochastic DO level-set optimization identifies energy-optimal vehicle speed functions for a wide range of arrival times.

6.2. Energy-optimal path planning in a double-gyre barotropic quasi-geostrophic ocean circulation

We now consider PDE simulations of the idealized near-surface wind-driven barotropic quasi-geostrophic double-gyre ocean circulation at mid-latitudes. The winds (e.g., mid-latitude easterlies and

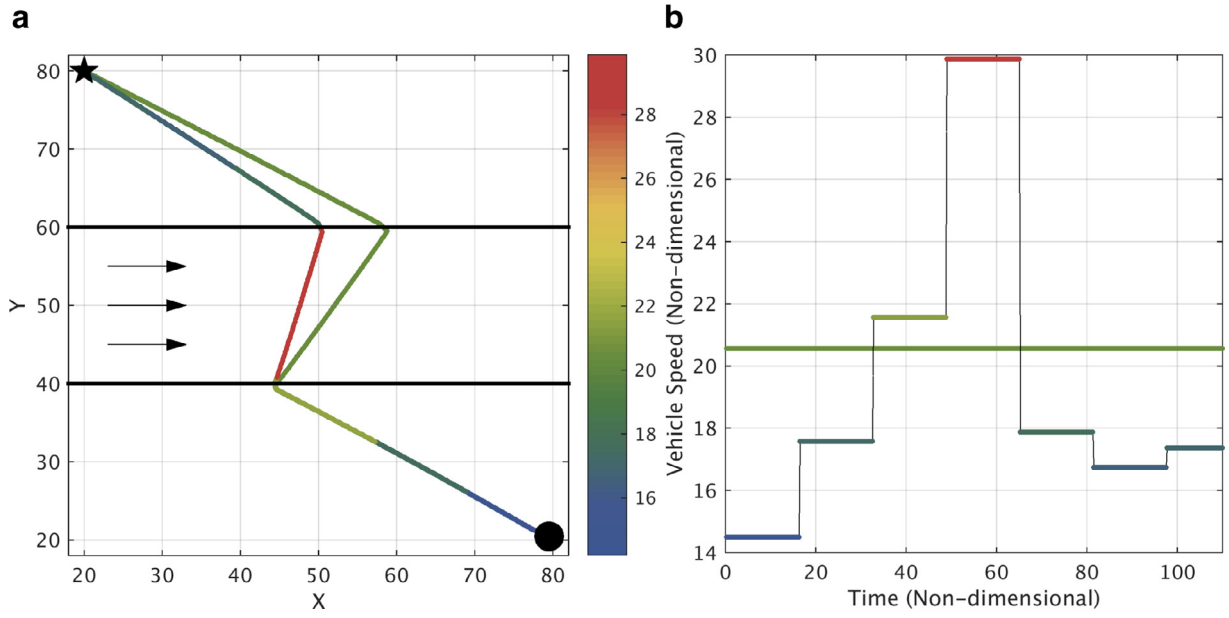

Fig. 10. *Crossing the front-upstream:* as Fig. 8a– b, but for the second mission against the flow. (a) Physical paths followed by a constant speed vehicle and by the energy optimal vehicle, for the same arrival time $T = 110$. Both are also time optimal paths for their respective speeds. (b) These instantaneous vehicle speed functions $F(t; r)$, for each of the two vehicles.

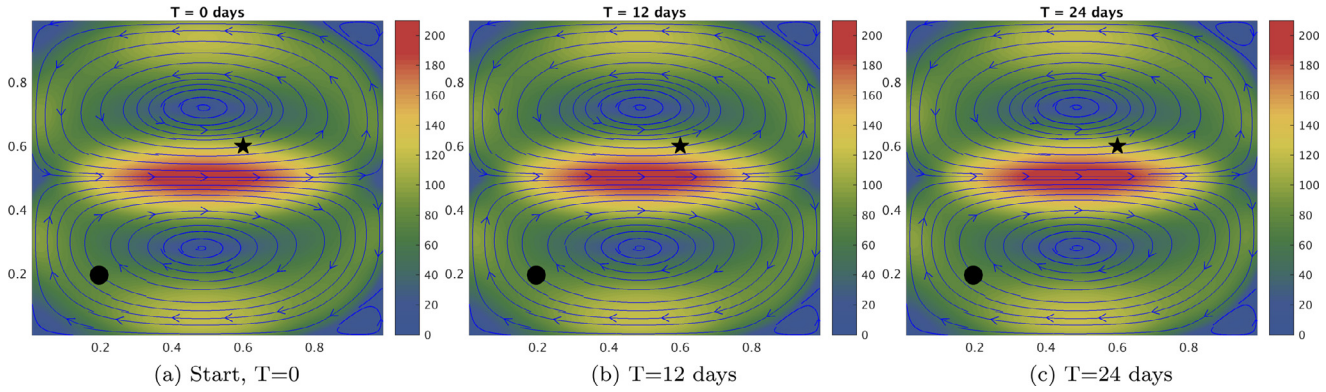

Fig. 11. Snapshots of the dynamic double-gyre flow, for a 1000 km × 1000 km grid simulation of 24 days. Flow patterns are illustrated by their streamlines, overlaid on a color plot of the flow magnitude (in cm/s). The x–axis and y–axis have units of 1000 km. For our energy-optimal mission, the circle is the start point and the star is the target.

trade winds in the northern hemisphere) drive a zonal jet eastward (e.g., the Gulf Stream or Kuroshio) with a cyclonic gyre to its north and an anticyclonic gyre to its south. Such a circulation is governed by the following barotropic quasi-geostrophic model (Dijkstra and Katsman, 1997; Pedlosky, 1998; Simmonet et al., 2009; Cushman-Roisin and Beckers, 2011), in the non-dimensional conservation of momentum form,

$$\frac{\partial u}{\partial t} = -\frac{\partial p}{\partial x} + \frac{1}{\mathrm{Re}}\nabla^2 u - \frac{\partial (u^2)}{\partial x} - \frac{\partial (uv)}{\partial y} + fv + a\tau_x, \tag{31a}$$

$$\frac{\partial v}{\partial t} = -\frac{\partial p}{\partial y} + \frac{1}{\mathrm{Re}}\nabla^2 v - \frac{\partial (vu)}{\partial x} - \frac{\partial (v^2)}{\partial y} - fu + a\tau_y, \tag{31b}$$

$$0 = \frac{\partial u}{\partial x} + \frac{\partial v}{\partial y}, \tag{31c}$$

where Re is the flow Reynolds number based on eddy-viscosity taking values from 10 to 10^4, $f = \tilde{f} + \beta y$ the non-dimensional Coriolis coefficient, and $a = 10^3$ the strength of the wind stress. In our illustration, we employ Re = 1000 (other results not shown). For the Coriolis coefficient, we set the non-dimensional numbers as $\tilde{f} = 0,\ \beta = 10^3$. The flow in the basin is forced by an idealized steady zonal wind stress, $\tau_x = -\frac{1}{2\pi}\cos 2\pi y$ and $\tau_y = 0$. The horizontal length scale is $L = 10^6$ m, vertical depth scale $D = 1000$ m, velocity scale 1.98 cm/s, eddy viscosity 19.77 m^2/s, time scale T = 1.6 yrs, and $\beta_0 = 1.977$ e -19 ms.

The above PDEs are solved by a Finite Volume framework (Ueckermann and Lermusiaux, 2011). Free slip boundary conditions are imposed on the northern and southern walls ($y = 0, 1$) and no-slip boundary conditions on the eastern and western walls ($x = 0, 1$). A 64 × 64 grid and a non-dimensional time step of 10^{-5} are used to solve both the flow field PDEs (31) and stochastic DO level-set PDEs (21)–(23) using the *DO–Taylor Gamma* variant. We use $n_r = 65,536$ and $n_{s,\phi} = n_{s,\gamma} = 20$. The flow simulation is first run for a duration equal to the main time scale, i.e., 1.6 yrs. The flow for the next 24 days is considered for our mission. The double-gyre flow field for the mission's duration is illustrated in Fig. 11.

Crossing the zonal jet in the double-gyre ocean circulation. The mission starts from the south of the zonal jet in the anticyclonic region and ends at a point north of the zonal jet in the cyclonic

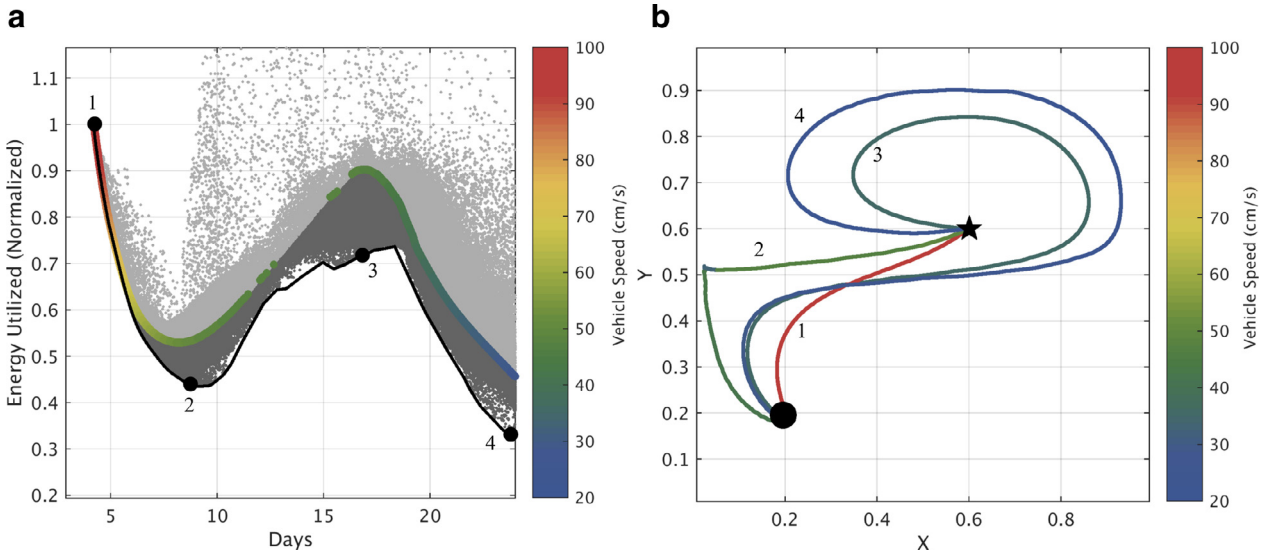

Fig. 12. (a) Energy-time-vehicle-speed distribution for different realizations of vehicle speeds, $F(t; r)$. Each dot represents a unique sample r of $F(t; r)$. The stochastic DO level–set simulation generates such a distribution in a single solve. Colored dots are constant speed samples overlaid by their respective vehicle speeds. The dark (light) gray dots are realizations that consume less (more) energy than constant speed realizations but reach in the same time. The lowest energy envelope is shown by a thick black line. Next, we perform the energy optimization among all realizations, for as many arrival times as needed. (b) Energy optimal trajectories that reach at four of such arrival times. Path 1 requires the most energy and least time to reach. Path 4 consumes the least energy but takes maximum time. Path 3 consumes more energy and takes more time than path 2. This is because path 3 has to follow a "loop" to catch the cyclonic gyre to reach the target.

region. The zonal jet velocity is strongest in the middle of the domain and weaker closer to the east and west boundaries, where it either originates from the two gyres or feeds the two gyres. Intuitively, we can thus expect that some vehicles that *ride* the gyres and cross the zonal jet in these regions of minimum resistance may consume less energy than vehicles that cross the strongest portion of zonal jet. Indeed this is what we observe.

Specifically, the vehicle starts from the point (0.2,0.2) and the target is the point (0.6,0.6). Stochastic vehicle speeds are sampled from the switch sampling procedure (e.g., Fig. 4) and used as forcing for the stochastic DO simulation. Fig. 12a shows the resulting distribution of energy and time to reach for each realization. Each dot represents a particular sample simulated by the DO equations. Special emphasis is placed on constant speed samples: they are colored with their respective speeds and the goal is to compute the paths that reduce their energy usage. For each discrete arrival time, or a range of arrival times, the dot (i.e., the realization) minimizing energy usage can be obtained by searching for the minima among all the dots (i.e., the realizations) that have the same arrival time(s) but more efficient vehicle speed specifications.

First, analyzing the energy-time curve for constant speed vehicles, we notice that, initially, reducing the vehicle speed reduces the energy consumption and increases travel time. However, after about 8 days, as the speed is reduced, the energy consumption increases. We also find that the constant speed samples have missing ranges of arrival times. These *holes* correspond to bifurcation regions in the level-set dynamics (A.1). By reducing its speed any further, the vehicle has to take a longer path that consumes more energy. After the local maxima in energy requirement, further reduction in vehicle speeds results again in a more intuitive decreased energy usage. Note that all vehicles arriving in this time range travel a longer path.

Second, analyzing the variable speed paths, they show similar behavior but have a complete range of arrival times, i.e., there is no *hole* in possible arrival times. Moreover, for arrival times shorter than 6 days, a variable speed path does not reduce the energy usage of a constant speed vehicle. For travel times greater than 6 days, many variable speed paths consume less energy. The stochastic DO optimization method then obtains the paths among these that require minimum energy.

Fig. 12b we show the optimal trajectories that reach in 4 days (marked as 1), 9 days (marked as 2), 17 days (marked as 3), and 24 days (marked as 4). Path 1 requires the most energy and least time to complete the mission. Path 4 is the least energy consuming but takes maximum time. Path 3 consumes more energy and takes more time than path 2 due to the nature of the double–gyre flow that forces path 3 to perform a *loop* and catch the cyclonic gyre to arrive at the target. These paths save 20% to 30% energy compared to the constant speed paths that arrive at the same time. Path 4 saves 68% energy compared to path 1, but takes 6 times the amount of time required to complete the mission. In ocean applications where endurance has to be increased and more area covered, path 4 or any other path corresponding to realizations on the minimum envelope may be preferred. Of course, if the two gyres were asymmetric in their strength of circulation as for the North Atlantic gyre system (e.g., Gangopadhyay et al., 1997; Dijkstra and Molemaker, 1999), for several start and end point configurations, the energy optimal paths would prefer to *ride* the stronger gyre to reduce energy utilization.

Discussion. Inspired by the double-gyre results, a key question is how can the energy-optimal paths be used in real applications. One approach is to utilize them as open-loop forecasts: the energy-optimal paths are then forecast for the set of vehicles available, using data-assimilative ocean forecasts as inputs, e.g., see (Subramani et al., 2016). Then, as the vehicles operate, if they re-surface or are in communication range, the new data collected and new forecasts can be combined, and the energy-optimal paths re-computed. A second approach is a data-only scheme, where the vehicle builds the local flow fields based on its measurements only. Our optimization can then be run based on this flow field representation, either onboard the vehicles or remotely if vehicles can communicate every so often. Of course, today, the idea that only local ocean data or only analytical models are available to make an optimal decision is obsolete. Instead, all information is combined using uncertainty quantification and data assimilation.

7. Conclusions

A stochastic dynamically orthogonal (DO) level-set optimization methodology was formulated for energy-optimal path planning of vehicles navigating in dynamic flows. It computes relative vehicle speeds and headings that minimize energy consumption, optimizing among all time-optimal paths for a range of arrival times. A new premise was to consider vehicle-speeds and headings to be both time-dependent and stochastic. Stochastic DO level-set PDEs were then derived, introducing a DO decomposition for the stochastic level-set fields. Three variants of the DO equations were developed, each of which handle the non-polynomial nonlinearity arising from the normal to the level-sets differently. Integrating the DO level-set PDEs provides the joint energy-time-vehicle-speed distribution. For a queried time (or range of time) to reach, an optimization is then performed on the marginal energy-vehicle-speed distribution so as to identify the minimum energy realization. The energy-optimal paths are finally computed by solving a particle backtracking ODE. Numerical schemes and algorithms for the DO level-set PDEs were discussed and illustrated. The new PDEs and the overall optimization methodology were validated and their respective accuracy studied. To illustrate the energy-optimal path planning and showcase its properties for ocean missions, examples were provided for steady fronts and dynamic quasi-geostrophic double-gyre flows.

The DO level-set PDEs were found efficient at solving the governing stochastic equations by comparing their solutions with those of direct Monte Carlo simulations. First, the DO PDEs provided a major computational advantage over direct Monte Carlo, in our examples, a 100-to-10,000 speed up. Second, they provided accurate solutions. In our examples, the Frechet distances between the level-set contours computed by the two methods were within the spatial resolution and the arrival time distribution had less than 2% error for 99.5% of the samples. To validate the optimization methodology and illustrate its accuracy, we obtained a *semi-analytical* solution for the crossing of a uniform steady front, using a nonlinear double-optimization process. For the more complex dynamic double-gyre circulation, we confirmed that constant speed vehicles cannot reach their target within specific times if their speed is too small with respect to ocean currents. However, we showed that variable-speed vehicles can reach many more locations by saving energy in favorable currents and expending energy in unfavorable currents. We also found that the energy–optimal paths, which in our solution are also time–optimal, can have complex optimum curves of minimum-energy versus optimal-arrival-time. For example, this minimum energy could increase as the maximum vehicle speed decreased. This is because as the speed decreases, the variability of ocean currents can lead to significant lengthening of the optimal paths.

In the future, our methodology can be applied to plan energy-optimal paths in data-assimilative forecasts of realistic ocean currents (Haley and Lermusiaux, 2010; Subramani, 2014; Subramani et al., 2016). Another research direction is to account for the uncertainty of ocean forecasts and thus predict energy-optimal paths for stochastic flow fields (Wei, 2015). Overall, such combination

of ocean modeling with a PDE–based energy-minimization for autonomous vehicles holds much promise. This is especially true for long-duration ocean observing and monitoring, both of which are essential to understand and protect the ocean.

Acknowledgments

We thank the members of our MSEAS group particularly Drs. T. Lolla and P. Haley for useful discussions. We are grateful to the Office of Naval Research for research support under grants N00014-09-1-0676 (Science of Autonomy - A-MISSION) and N00014-14-1-0476 (Science of Autonomy - LEARNS) to the Massachusetts Institute of Technology. We also thank the three anonymous reviewers for their helpful comments.

Appendix A. Level-set equations governing time–optimal path planning

In this appendix, we provide the deterministic level-set equations that govern the time-optimal reachability front as well as the differential equation governing the time-optimal paths. Osher and Sethian (1988) introduced the use of level-set methods as a numerical framework for front evolution and tracking. The level-set of a function $f(\mathbf{x})$, $\mathbf{x} \in \mathbb{R}^n$, is defined as the set of points at which the function takes a given constant value, i.e., it is the set $\{\mathbf{x}|f(\mathbf{x}) = C\}$ where C is a given constant. For a general reference on level–set methods for interface tracking, we refer to Sethian (1999b). In Lolla (2012), Lolla et al. (2012), Lolla et al. (2014b), Lolla et al. (2014c), such level-set ideas are utilized to evolve the reachability front of autonomous vehicles navigating in any bounded flow field and thereby obtain a new methodology for time-optimal path planning in dynamic flows. Specifically, the time-optimal level-set evolves normal to itself at a nominal (engine) speed F and gets advected by the underlying flow field $\mathbf{v}(\mathbf{x}, t)$, overall as follows,

$$\frac{\partial \phi}{\partial t} + F|\nabla\phi| + \mathbf{v}(\mathbf{x}, t) \cdot \nabla\phi = 0. \tag{A.1}$$

The equation so developed is a Hamilton-Jacobi equation and the scalar level-set field, ϕ, is its viscosity solution, initialized with a signed distance function from the starting point. The authors prove that the points inside the zero level–set contour, i.e., corresponding to $\phi < 0$, constitute the reachability set and that the zero level-set is the reachability front for a vehicle of nominal vehicle-speed F. This provides an elegant and efficient method to predict the locations reachable by a vehicle over time. The authors also show that vehicles with a heading angle normal to the evolving level-set correspond to time-optimal paths. The optimal path that reaches the specified end point ($\mathbf{x_f}$) is then governed by the following kinematic equation,

$$\frac{d\mathbf{x}^*}{dt} = -\mathbf{v}(\mathbf{x}^*, t) - F\frac{\nabla\phi(\mathbf{x}^*, t)}{|\nabla\phi(\mathbf{x}^*, t)|}, \quad 0 \le t \le T(\mathbf{x_f}; F) \quad \text{and}$$
$$\mathbf{x}^*(T) = \mathbf{x_f}. \tag{A.2}$$

which is integrated backward in time from the target, as for a particle backtracking.

This level-set methodology (A.1)–(A.2) was applied to time-optimal path planning in realistic ocean flow fields (Lolla et al., 2014a) and extended to coordinated path planning and dynamic obstacles (Lolla et al., 2015). Using non–smooth calculus, Lolla and Lermusiaux (2016) rigorously generalize the level–set equation for the minimum–time control of anisotropic vehicles.

Appendix B. Mathematical derivation of DO equations

In this appendix, we derive the new DO level set equations obtained in Section 3.2.

B1. DO–MC Gamma derivation

We first derive Eqs. (17) to (19). Starting from the level set S-PDE given by (5), substituting the DO expansions for F (14) and ϕ (15), we obtain,

$$\frac{\partial\bar{\phi}}{\partial t} + Y_i\frac{\partial\tilde{\phi}_i}{\partial t} + \tilde{\phi}_i\frac{dY_i}{dt} = -(\bar{F} + z\tilde{F})\gamma - \mathbf{v}\cdot\nabla(\bar{\phi} + Y_i\tilde{\phi}_i). \tag{B.1}$$

The PDE for the mean is obtained from the expectation of (B.1)

$$\frac{\partial\bar{\phi}}{\partial t} = -(\bar{F}\mathbb{E}[\gamma] + \tilde{F}\mathbb{E}[z\gamma]) - \mathbf{v}\cdot\nabla\bar{\phi}. \tag{B.2}$$

The S-ODEs for the coefficients are obtained by taking the inner product of (B.1) with any of the modes,

$$\left\langle\frac{\partial\bar{\phi}}{\partial t}, \tilde{\phi}_n\right\rangle + Y_i\left\langle\frac{\partial\tilde{\phi}_i}{\partial t}, \tilde{\phi}_n\right\rangle + \left\langle\tilde{\phi}_i, \tilde{\phi}_n\right\rangle\frac{dY_i}{dt}$$
$$= -\left\langle\bar{F}\gamma - \tilde{F}z\gamma, \tilde{\phi}_n\right\rangle - \left\langle\mathbf{v}\cdot\nabla\bar{\phi} - Y_i\mathbf{v}\cdot\nabla\tilde{\phi}_i, \tilde{\phi}_n\right\rangle. \tag{B.3}$$

The first term on the LHS of (B.3) is then expanded by taking an inner product of (B.2) with the modes,

$$\left\langle\frac{\partial\bar{\phi}}{\partial t}, \tilde{\phi}_n\right\rangle = -\left\langle(\bar{F}\mathbb{E}[\gamma] + \tilde{F}\mathbb{E}[z\gamma]) + \mathbf{v}\cdot\nabla\bar{\phi}, \tilde{\phi}_n\right\rangle. \tag{B.4}$$

Substituting (B.4) into (B.3) and applying the dynamically orthogonal condition (8) yields,

$$Y_i\left\langle\frac{\partial\tilde{\phi}_i}{\partial t}, \tilde{\phi}_n\right\rangle + \left\langle\tilde{\phi}_i, \tilde{\phi}_n\right\rangle\frac{dY_i}{dt} = -\left\langle\bar{F}(\gamma - \mathbb{E}[\gamma]) + \tilde{F}(z\gamma - \mathbb{E}[z\gamma]) + Y_i\mathbf{v}\cdot\nabla\tilde{\phi}_i, \tilde{\phi}_n\right\rangle \tag{B.5}$$

$$\frac{dY_i}{dt} = -\left\langle\bar{F}(\gamma - \mathbb{E}[\gamma]) + \tilde{F}(z\gamma - \mathbb{E}[z\gamma]) + Y_k\mathbf{v}\cdot\nabla\tilde{\phi}_k, \tilde{\phi}_i\right\rangle, \tag{B.6}$$

where (B.6) is obtained from (B.5) because of the orthogonality of modes.

The PDEs for the DO modes are obtained by multiplying both sides of (B.1) with any of the coefficients and taking expectation (in duality with the above multiplication by the modes and spatial integration),

$$Y_j\frac{\partial\bar{\phi}}{\partial t} + Y_jY_i\frac{\partial\tilde{\phi}_i}{\partial t} + \tilde{\phi}_iY_j\frac{dY_i}{dt}$$
$$= -(Y_j\gamma\bar{F} + zY_j\gamma\tilde{F}) - Y_j\mathbf{v}\cdot\nabla\bar{\phi} - Y_jY_i\mathbf{v}\cdot\nabla\tilde{\phi}_i \tag{B.7}$$

$$C_{Y_jY_i}\frac{\partial\tilde{\phi}_i}{\partial t} + \tilde{\phi}_iC_{Y_j\frac{dY_i}{dt}} = -\bar{F}\mathbb{E}[Y_j\gamma] - \tilde{F}\mathbb{E}[zY_j\gamma] - C_{Y_jY_i}\mathbf{v}\cdot\nabla\tilde{\phi}_i. \tag{B.8}$$

In (B.8), $C_{Y_j\frac{dY_i}{dt}}$ is obtained by multiplying (B.6) with the coefficients and taking an expectation,

$$Y_j\frac{dY_i}{dt} = -\langle(Y_j\gamma - Y_jE[\gamma])\bar{F}, \tilde{\phi}_i\rangle$$
$$- \langle(zY_j\gamma - Y_jE[z\gamma])\tilde{F}, \tilde{\phi}_i\rangle - Y_jY_k\langle\mathbf{v}\cdot\nabla\tilde{\phi}_k, \tilde{\phi}_i\rangle \tag{B.9}$$

$$C_{Y_j\frac{dY_i}{dt}} = -\langle E[Y_j\gamma]\bar{F}, \tilde{\phi}_i\rangle - \langle E[zY_j\gamma])\tilde{F}, \tilde{\phi}_i\rangle$$
$$- C_{Y_jY_k}\langle\mathbf{v}\cdot\nabla\tilde{\phi}_k, \tilde{\phi}_i\rangle. \tag{B.10}$$

Substituting (B.10) into (B.8) yields the final evolution PDEs for the DO modes,

$$\frac{\partial\tilde{\phi}_i}{\partial t} = -C^{-1}_{Y_iY_j}E[Y_j\gamma]\bar{F} - C^{-1}_{Y_iY_j}E[zY_j\gamma]\tilde{F} - \mathbf{v}\cdot\nabla\tilde{\phi}_i$$
$$- \langle(-C^{-1}_{Y_iY_j}E[Y_j\gamma]\bar{F} - C^{-1}_{YikY_j}E[zY_j\gamma]\tilde{F} - \mathbf{v}\cdot\nabla\tilde{\phi}_i), \tilde{\phi}_n\rangle\tilde{\phi}_n\ . \tag{B.11}$$

B2. DO-KL Gamma and DO-Taylor Gamma Derivation

We now show the key steps required to obtain Eqs. (21) to (23). Introducing the DO expansion for γ (20) in (B.1), we obtain the S-PDE,

$$\begin{aligned}\frac{\partial\bar{\phi}}{\partial t}+Y_i\frac{\partial\tilde{\phi}_i}{\partial t}+\tilde{\phi}_i\frac{dY_i}{dt} &= -(\bar{F}+z\tilde{F})(\bar{\gamma}+\alpha_i\tilde{\gamma}_i)-\mathbf{v}\cdot\nabla(\bar{\phi}+Y_i\tilde{\phi}_i)\\ &= -(\bar{F}\bar{\gamma}+\bar{F}\alpha_i\tilde{\gamma}_i+z\tilde{F}\bar{\gamma}+z\alpha_i\tilde{\gamma}_i\tilde{F})\\ &\quad -\mathbf{v}\cdot\nabla(\bar{\phi}+Y_i\tilde{\phi}_i)\end{aligned} \tag{B.12}$$

The corresponding PDE for the mean is obtained from the expectation of (B.12),

$$\frac{\partial\bar{\phi}}{\partial t}=-(\bar{F}\bar{\gamma}+\tilde{F}\mathbb{E}[z\alpha_i]\tilde{\gamma}_i)-\mathbf{v}\cdot\nabla\bar{\phi}. \tag{B.13}$$

To obtain the coefficients S-ODEs, we take the inner product of (B.12) with any of the modes $\tilde{\phi}_n$,

$$\begin{aligned}&\left\langle\frac{\partial\bar{\phi}}{\partial t},\tilde{\phi}_n\right\rangle+Y_i\left\langle\frac{\partial\tilde{\phi}_i}{\partial t},t\right\rangle+\left\langle\tilde{\phi}_i,\tilde{\phi}_n\right\rangle\frac{\mathrm{d}Y_i}{\mathrm{d}t}\\ &\quad=-\left\langle\bar{F}\bar{\gamma}+\bar{F}\alpha_i\tilde{\gamma}_i+z\tilde{F}\bar{\gamma}+z\tilde{F}\alpha_i\tilde{\gamma}_i,\tilde{\phi}_n\right\rangle\\ &\qquad-\left\langle\mathbf{v}\cdot\nabla\bar{\phi}+Y_i\mathbf{v}\cdot\nabla\tilde{\phi}_i,\tilde{\phi}_n\right\rangle.\end{aligned} \tag{B.14}$$

The first term of the LHS of (B.14) can be obtained by taking an inner product of (B.13) with $\tilde{\phi}_n$,

$$\left\langle\frac{\partial\bar{\phi}}{\partial t},\tilde{\phi}_n\right\rangle=-\left\langle\bar{F}\bar{\gamma}+\tilde{F}\mathbb{E}[z\alpha_i]\tilde{\gamma}_i+\mathbf{v}\cdot\nabla\bar{\phi},\tilde{\phi}_n\right\rangle. \tag{B.15}$$

Next, substituting (B.15) in (B.14) and using the dynamical orthogonality condition (8) yields,

$$\left\langle\tilde{\phi}_i,\tilde{\phi}_n\right\rangle\frac{\mathrm{d}Y_i}{\mathrm{d}t}=-\left\langle\bar{F}\alpha_i\tilde{\gamma}_i+\tilde{F}z\bar{\gamma}+\tilde{F}(z\alpha_i-\mathbb{E}[z\alpha_i])\tilde{\gamma}_i+Y_i\mathbf{v}\cdot\nabla\tilde{\phi}_i,\tilde{\phi}_n\right\rangle. \tag{B.16}$$

Using the orthogonality of modes, we finally obtain the coefficients S-ODEs,

$$\frac{\mathrm{d}Y_i}{\mathrm{d}t}=-\left\langle\bar{F}\alpha_k\tilde{\gamma}_k+\tilde{F}z\bar{\gamma}+\tilde{F}(z\alpha_k-\mathbb{E}[z\alpha_k])\tilde{\gamma}_k+Y_k\mathbf{v}\cdot\nabla\tilde{\phi}_k,\tilde{\phi}_i\right\rangle. \tag{B.17}$$

For the PDEs for the modes, we multiply (B.12) with coefficients Y_j and take the expectation to get,

$$\begin{aligned}&C_{Y_jY_i}\frac{\partial\tilde{\phi}_i}{\partial t}+\tilde{\phi}_iC_{Y_j\frac{\mathrm{d}Y_i}{\mathrm{d}t}}=-\mathbb{E}[Y_j\alpha_i]\tilde{\gamma}_i\bar{F}\\ &-C_{Y_jz}\bar{F}\bar{\gamma}-\mathbb{E}[Y_jz\alpha_i]\tilde{\gamma}_i\tilde{F}-C_{Y_jY_i}\mathbf{v}\cdot\nabla\tilde{\phi}_i.\end{aligned} \tag{B.18}$$

In (B.18), $C_{Y_j\frac{\mathrm{d}Y_i}{\mathrm{d}t}}$ is obtained by multiplying (B.17) with Y_j and taking an expectation,

$$C_{Y_j\frac{\mathrm{d}Y_i}{\mathrm{d}t}}=-\left\langle\bar{F}\mathbb{E}[Y_j\alpha_k]\tilde{\gamma}_k+\tilde{F}\mathbb{E}[Y_jz\alpha_k]\tilde{\gamma}_k+C_{Y_jY_k}\mathbf{v}\cdot\nabla\tilde{\phi}_k+C_{Y_jz}\tilde{F}\bar{\gamma},\tilde{\phi}_i\right\rangle. \tag{B.19}$$

Substituting (B.19) in (B.18) and rearranging, we obtain the PDEs for the modes,

$$\begin{aligned}\frac{\partial\tilde{\phi}_i}{\partial t}&=-C^{-1}_{Y_iY_j}(\mathbb{E}[Y_j\alpha_k]\tilde{\gamma}_k\bar{F}+C_{Y_jz}\tilde{F}\bar{\gamma}+\mathbb{E}[Y_jz\alpha_k]\tilde{\gamma}_k\tilde{F})-\mathbf{v}\cdot\nabla\tilde{\phi}_i\\ &\quad-\left\langle-C^{-1}_{Y_iY_j}(\mathbb{E}[Y_j\alpha_k]\tilde{\gamma}_k\bar{F}+C_{Y_jz}\tilde{F}\bar{\gamma}+\mathbb{E}[Y_jz\alpha_k]\tilde{\gamma}_k\tilde{F})-\mathbf{v}\cdot\nabla\tilde{\phi}_i,\tilde{\phi}_n\right\rangle\tilde{\phi}_n.\end{aligned} \tag{B.20}$$

B2.1. DO-KL Gamma: KL decomposition of γ

Mean, modes and coefficients of γ are obtained from γ realizations computed from ϕ realizations. Defining the mean as

$$\bar{\gamma}=\mathbb{E}[|\nabla(\bar{\phi}+Y_i\tilde{\phi}_i)|] \tag{B.21}$$

we obtain the ensemble spread matrix for γ (matrix of mean–removed γ^r realizations),

$$M\equiv\begin{bmatrix}|\nabla(\bar{\phi}+Y_i^1\tilde{\phi}_i)|-\bar{\gamma} & |\nabla(\bar{\phi}+Y_i^2\tilde{\phi}_i)|-\bar{\gamma} & \cdots & |\nabla(\bar{\phi}+Y_i^{n_r}\tilde{\phi}_i)|-\bar{\gamma}\\ \vdots & \vdots & \vdots & \vdots\end{bmatrix} \tag{B.22}$$

where the superscript on Y_i refers to the realization number and n_r is the total number of realizations. Taking the SVD of these zero–mean realizations, we obtain,

$$M=USV^T \tag{B.23}$$

$$\alpha=VS^T \tag{B.24}$$

$$\tilde{\gamma}=U \tag{B.25}$$

B2.2. DO-Taylor Gamma: Taylor series for γ

To obtain the first order Taylor approximation for the non-polynomial non-linearity and corresponding results (see Section 3.2.2), we consider γ as a function of realizations of spatial derivatives,

$$f(\phi_x,\phi_y)=\sqrt{\phi_x^2+\phi_y^2}. \tag{B.26}$$

The corresponding first order Taylor approximation is then obtained as,

$$\gamma=f(\phi_x,\phi_y) \tag{B.27}$$

$$=f(\bar{\phi}_x+Y_i\tilde{\phi}_{i_x},\bar{\phi}_x+Y_i\tilde{\phi}_{i_y}) \tag{B.28}$$

$$=f(\bar{\phi}_x,\bar{\phi}_y)+Y_i\left(\tilde{\phi}_{i_x}\frac{\partial f(\bar{\phi}_x,\bar{\phi}_y)}{\partial\bar{\phi}_x}+\tilde{\phi}_{i_y}\frac{\partial f(\bar{\phi}_x,\bar{\phi}_y)}{\partial\bar{\phi}_y}\right). \tag{B.29}$$

This allows us to obtain the results presented in Section 3.2.2, specifically,

$$\begin{aligned}\bar{\gamma}&=f(\bar{\phi}_x,\bar{\phi}_y)\\ &=\sqrt{\bar{\phi}_x^2+\bar{\phi}_y^2}\end{aligned} \tag{B.30}$$

$$\alpha_i=Y_i \tag{B.31}$$

$$\begin{aligned}\tilde{\gamma}_i&=\tilde{\phi}_{i_x}\frac{\partial f(\bar{\phi}_x,\bar{\phi}_y)}{\partial\bar{\phi}_x}+\tilde{\phi}_{i_y}\frac{\partial f(\bar{\phi}_x,\bar{\phi}_y)}{\partial\bar{\phi}_y}\\ &=\tilde{\phi}_{i_x}\frac{\bar{\phi}_x}{\sqrt{\bar{\phi}_x^2+\bar{\phi}_y^2}}+\tilde{\phi}_{i_y}\frac{\bar{\phi}_y}{\sqrt{\bar{\phi}_x^2+\bar{\phi}_y^2}}\end{aligned} \tag{B.32}$$

where the subscript x and y refer to derivatives with respect to x and y.

Appendix C. Notation and abbreviations

Here we provide all the notation and acronyms (Table C.5) used in the present paper.

Table C.5
Notation and acronyms relevant to the stochastic DO level–set optimization.

Scalar		
i	$\in \mathbb{N}$	Stochastic subspace index
F	$\in \mathbb{R}$	Vehicle speed
$\bar{F}$	$\in \mathbb{R}$	Mean vehicle speed
$\tilde{F}$	$\in \mathbb{R}$	DO mode of F
n_g	$\in \mathbb{N}$	Total number of grid points (Dimension of state vector)
$n_{s,\,\phi}$	$\in \mathbb{N}$	Dimension of the stochastic subspace of level-set
$n_{s,\,\gamma}$	$\in \mathbb{N}$	Dimension of the stochastic subspace of γ (defined below), the non-polynomial nonlinearity.
$n_{s,\,F}$	$\in \mathbb{N}$	Dimension of the stochastic subspace (in time) of the time dependent vehicle speed
Y_i	$\in \mathbb{R}$	Random variable describing the pdf of the orthonormal level-set(ϕ) modes $\tilde{\phi}_i$
α_i	$\in \mathbb{R}$	Random variable describing the pdf of the orthonormal γ-modes, $\tilde{\gamma}_i$
z	$\in \mathbb{R}$	Random variable describing the pdf of the vehicle speed F
n_r	$\in \mathbb{N}$	Number of Monte Carlo realizations of the level–sets (and vehicle speeds).
n_p	$\in \mathbb{N}$	Power function dependence of vehicle speed
$n_{sw,F}$	$\in \mathbb{N}$	Number of switches made in the vehicle speed throughout the duration of the simulation for the switch-sampling algorithm
l	$\in \mathbb{N}$	Number of discrete levels into which the vehicle speed spread is divided for the switch–sampling algorithm
r	$\in \mathbb{N}$	Realization index
T	$\in \mathbb{R}^+$	Optimal arrival time random variable
Vector		
$\boldsymbol{\phi}$	$\in \mathbb{R}^{n_g}$	Level-Set field
$\bar{\boldsymbol{\phi}}$	$\in \mathbb{R}^{n_g}$	Mean Level-Set field
$\tilde{\boldsymbol{\phi}}_i$	$\in \mathbb{R}^{n_g}$	DO mode i of ϕ: Dynamically orthogonal basis for the stochastic subspace of ϕ
$\boldsymbol{\gamma}$	$\in \mathbb{R}^{n_g}$	$\lvert\nabla\phi\rvert$
$\bar{\boldsymbol{\gamma}}$	$\in \mathbb{R}^{n_g}$	Mean γ
$\tilde{\boldsymbol{\gamma}}_i$	$\in \mathbb{R}^{n_g}$	DO mode i of γ: Dynamically orthogonal basis for the stochastic subspace of γ
Acronyms		
DO		Dynamically Orthogonal
KL		Karhunen-Loéve
MC		Monte Carlo
ODE		Ordinary Differential Equation
PDE		Partial Differential Equation
PDF		Probability Density Function
S–PDE		Stochastic Partial Differential Equation γ
SVD		Singular Vector Decomposition

References

Aghababa, M.P., 2012. 3d path planning for underwater vehicles using five evolutionary optimization algorithms avoiding static and energetic obstacles. Appl. Ocean Res. 38, 48–62.

Alt, H., Godau, M., 1995. Computing the fréchet distance between two polygonal curves. Int. J. Comput. Geomet. Appl. 5 (01n02), 75–91. doi:10.1142/S0218195995000064.

Alvarez, A., Caiti, A., Onken, R., 2004. Evolutionary path planning for autonomous underwater vehicles in a variable ocean. IEEE J. Ocean Eng 29 (2), 418–429.

Athans, M., Falb, P., 2007. Optimal control: an introduction to the theory and its applications. Dover Books on Engineering Series. Dover Publications, New York.

Bachmayer, R., Leonard, N.E., Graver, J., Fiorelli, E., Bhatta, P., Paley, D., 2004. Underwater gliders: recent developments and future applications. In: IEEE International Symposium on Underwater Technology, UT '04. Taipei, Taiwan, pp. 195–200. doi:10.1109/UT.2004.1405540.

Bahr, A., Leonard, J.J., Fallon, M.F., 2009. Cooperative localization for autonomous underwater vehicles. Int. J. Robot. Res. 28 (6), 714–728.

Barraquand, J., Langlois, B., Latombe, J.C., 1992. Numerical potential field techniques for robot path planning. IEEE Trans. Syst., Man, Cybern. 22 (2), 224–241.

Bellingham, J.G., Rajan, K., 2007. Robotics in remote and hostile environments. Science 318 (5853), 1098–1102.

Beylkin, D., 2008. Path Optimization For An Earth-Based Demonstration Balloon Flight. SURF Report. Caltech, Pasadena, CA.

Bhatta, P., Fiorelli, E., Lekien, F., Leonard, N.E., Paley, D.A., Zhang, F., Bachmayer, R., Davis, R.E., Fratantoni, D.M., Sepulchre, R., 2005. Coordination of an underwater glider fleet for adaptive sampling. In: Proceedings of International Workshop on Underwater Robotics, pp. 61–69.

Bruce, J., Veloso, M., 2002. Real-time randomized path planning for robot navigation. In: Intelligent Robots and Systems, 2002. IEEE/RSJ International Conference on, 3. Switzerland, pp. 2383–2388. doi:10.1109/IRDS.2002.1041624.

Bryson, A.E., Ho, Y.C., 1975. Applied Optimal Control: Optimization, Estimation and Control. CRC Press, New York.

Carroll, K., McClaran, S., Nelson, E., Barnett, D., Friesen, D., William, G., 1992. AUV path planning: An A* approach to path planning with consideration of variable vehicle speeds and multiple, overlapping, time-dependent exclusion zones. In: Proceedings of the Symposium on Autonomous Underwater Vehicle Technology, pp. 79–84.

Chakrabarty, A., Langelaan, J., 2013. UAV flight path planning in time varying complex wind-fields. In: American Control Conference. IEEE, pp. 2568–2574.

Chien-Chou, S., Yih, Y., Mong-Fong, H., Tien-Szu, P., Jeng-Shyang, P., 2014. A framework to evolutionary path planning for autonomous underwater glider. In: Ali, M., Pan, J.-S., Chen, S.-M., Horng, M.-F. (Eds.), Modern Advances in Applied Intelligence. In: *Lecture Notes in Computer Science*, 8482. Springer International Publishing, pp. 1–11.

Curtin, T.B., Bellingham, J.G., 2009. Progress toward autonomous ocean sampling networks. Deep Sea Res. Part II: Top. Stud. Oceanogr. 56 (3), 62–67.

Cushman-Roisin, B., Beckers, J., 2011, 101. Introduction to Geophysical Fluid Dynamics. Physical and Numerical aspects. Academic Press, Waltham, MA.

Danziger, Z., 2011. MATLAB code for calculating discrete frechet distance. http://www.mathworks.com/matlabcentral/fileexchange/31922-discrete-frechet-distance, [Online; accessed 8-Aug-2014].

Debusschere, B.J., Najm, H.N., Pébay, P.P., Knio, O.M., Ghanem, R.G., Maître, O.P.L., 2005. Numerical challenges in the use of polynomial chaos representations for stochastic processes. SIAM J. Sci. Comput. 26 (2), 698–719.

Dijkstra, H., Katsman, C., 1997. Temporal variability of the wind-driven quasi-geostrophic double gyre ocean circulation: basic bifurcation diagrams. Geophys. Astrophys. Fluid Dyn. 85, 195–232.

Dijkstra, H.A., Molemaker, M.J., 1999. Imperfections of the north atlantic wind-driven ocean circulation: continental geometry and windstress shape. J. Mar. Res. 57 (1), 1–28.

Elisseeff, P., Schmidt, H., Johnson, M., Herold, D., Chapman, N.R., McDonald, M.M., 1999. Acoustic tomography of a coastal front in Haro Strait, British Columbia. J. Acoust. Soc. Am. 106 (1), 169–184. doi:10.1121/1.427046.

Eriksen, C.C., Osse, T.J., Light, R.D., Wen, T., Lehman, T.W., Sabin, P.L., Ballard, J.W., Chiodi, A.M., 2001. Seaglider: a long-range autonomous underwater vehicle for oceanographic research. IEEE J. Ocean Eng. 26 (4), 424–436.

Gangopadhyay, A., Robinson, A., Arango, H., 1997. Circulation and dynamics of the western north atlantic. part I: multiscale feature models. J. Atmosp. Oceanic Technol. 14 (6), 1314–1332.

Garau, B., Alvarez, A., Oliver, G., 2005. Path planning of autonomous underwater vehicles in current fields with complex spatial variability: an A* approach. In: Proceedings of the 2005 IEEE International Conference on Robotics and Automation. IEEE, pp. 194–198.

Garau, B., Bonet, M., Alvarez, A., Ruiz, S., Pascual, A., et al., 2009. Path planning for autonomous underwater vehicles in realistic oceanic current fields: Application to gliders in the western mediterranean sea. J. Marit. Res. 6 (2), 5–22.

Gelb, A., 1974. Applied Optimal Estimation. MIT press, Cambridge, MA.

Gomes, C.P., Sabharwal, A., Selman, B., 2006. Near-uniform sampling of combinatorial spaces using xor constraints. In: Advances In Neural Information Processing Systems, pp. 481–488.

Gugercin, S., 2005. An iterative svd-krylov based method for model reduction of large-scale dynamical systems. In: Proceedings of the 2005 European Control Conference on 44th IEEE Conference on Decision and Control, 2005 CDC-ECC'05. IEEE, pp. 5905–5910.

Gupta, A., Lin, J., Lermusiaux, P.F.J., Haley Jr., P.J., 2016. Bayesian Inference of Coupled Ocean Biogeochemical-Physical Models. MSEAS Report. Department of Mechanical Engineering, Massachusetts Institute of Technology. Cambridge, MA.

Haley Jr., P.J., Lermusiaux, P.F.J., 2010. Multiscale two-way embedding schemes for free-surface primitive equations in the "multidisciplinary simulation, estimation and assimilation system". Ocean Dyn. 60 (6), 1497–1537. doi:10.1007/s10236-010-0349-4.

Haley Jr., P.J., Lermusiaux, P.F.J., Robinson, A.R., Leslie, W.G., Logoutov, O., Cossarini, G., Liang, X.S., Moreno, P., Ramp, S.R., Doyle, J.D., Bellingham, J., Chavez, F., Johnston, S., 2009. Forecasting and reanalysis in the Monterey Bay/California Current region for the autonomous ocean sampling network-II experiment. Deep Sea Res. Part II: Top. Stud. Oceanogr. 56 (3–5), 127–148.10.1016/j.dsr2.2008.08.010

Hoare, C.A., 1962. Quicksort. Comput. J. 5 (1), 10–16.

Hsieh, M.A., Forgoston, E., Mather, T.W., Schwartz, I.B., 2012. Robotic manifold tracking of coherent structures in flows. In: Proceedings of the IEEE International Conference on Robotics and Automation. IEEE, pp. 4242–4247.

Hwang, Y.K., Ahuja, N., 1992. Gross motion planning – a survey. ACM Comput. Surv.(CSUR) 24 (3), 219–291.

Inanc, T., Shadden, S.C., Marsden, J.E., 2005. Optimal Trajectory Generation in Ocean Flows. In: Proceedings of American Control Conference, 1, pp. 674–679.

Jaillet, L., Cortés, J., Siméon, T., 2010. Sampling-based path planning on configuration-space costmaps. IEEE Trans. Robot. 26 (4), 635–646.

Julier, S.J., Uhlmann, J.K., 1996. A general method for approximating nonlinear transformations of probability distributions. Technical Report. Robotics Research Group, Department of Engineering Science, University of Oxford.

Karaman, Frazzoli, 2011. Sampling-based algorithms for optimal motion planning. Int. J. Robot. Res. 30 (7), 846–894.

Kavraki, L.E., Svestka, P., Latombe, J.-C., Overmars, M.H., 1996. Probabilistic roadmaps for path planning in high-dimensional configuration spaces. IEEE Trans. Robot. Autom. 12 (4), 566–580.

Kruger, D., Stolkin, R., Blum, A., Briganti, J., 2007. Optimal AUV path planning for extended missions in complex, fast-flowing estuarine environments. In: Proceedings of the IEEE International Conference on Robotics and Automation, 2007, pp. 4265–4270.

Kuffner, J.J., LaValle, S.M., 2000. RRT-connect: an efficient approach to single-query path planning. In: Proceedings of IEEE International Conference on Robotics and Automation, pp. 995–1001.

Latombe, J.-C., 1991. Robot Motion Planning. Kluwer Academic Publishers, New York.

LaValle, S.M., 1998. Rapidly-Exploring Random Trees: A New Tool for Path Planning. Technical Report. Iowa State University.

LaValle, S.M., 2006. Planning algorithms. Cambridge university press, Cambridge, UK.

LaValle, S.M., Hutchinson, S.A., 1998. Optimal motion planning for multiple robots having independent goals. IEEE Trans. Robot. Autom. 14 (6), 912–925.

Lee, T., Kim, H., Chung, H., Bang, Y., Myung, H., 2015. Energy efficient path planning for a marine surface vehicle considering heading angle. Ocean Eng. 107, 118–131.

Leonard, N.E., Paley, D.A., Davis, R.E., Fratantoni, D.M., Lekien, F., Zhang, F., 2010. Coordinated control of an underwater glider fleet in an adaptive ocean sampling field experiment in monterey bay. J. Field Robot. 27 (6), 718–740.

Lermusiaux, P.F.J., 1999. Estimation and study of mesoscale variability in the Strait of Sicily. Dyn. Atmosp. Oceans 29 (2), 255–303.

Lermusiaux, P.F.J., Lolla, T., Haley, P.J., Yiğit, K., Ueckermann, M.P., Sondergaard, T., Leslie, W.G., 2015. Science of Autonomy: time-optimal path planning and adaptive sampling for swarms of ocean vehicles. In: Curtin, T. (Ed.), Springer Handbook of Ocean Engineering: Autonomous Ocean Vehicles, Subsystems and Control. Springer-Verlag. in press (Ch. 11).

Lin, D., Fisher, J., 2012. Efficient sampling from combinatorial space via bridging. In: International Conference on Artificial Intelligence and Statistics, pp. 694–702.

Lolla, T., 2012. Path Planning in Time Dependent Flows using Level Set Methods. Department of Mechanical Engineering, Massachusetts Institute of Technology master's thesis.

Lolla, T., Haley Jr., P.J., Lermusiaux, P.F.J., 2014a. Time-optimal path planning in dynamic flows using level set equations: realistic applications. Ocean Dyn. 64 (10), 1399–1417.

Lolla, T., Haley Jr., P.J., Lermusiaux, P.F.J., 2015. Path planning in multi-scale ocean flows: Coordination and dynamic obstacles. Ocean Modell. 94, 46–66. doi:10.1016/j.ocemod.2015.07.013.

Lolla, T., Lermusiaux, P.F.J., 2016. A forward reachability equation for minimum-time path planning in strong dynamic flows. SIAM J. Control Optim..Sub–judice

Lolla, T., Lermusiaux, P.F.J., Ueckermann, M.P., Haley Jr., P.J., 2014b. Modified level set approaches for the planning of time-optimal paths for swarms of ocean vehicles. MSEAS Report. Department of Mechanical Engineering, Massachusetts Institute of Technology. Cambridge, MA.

Lolla, T., Lermusiaux, P.F.J., Ueckermann, M.P., Haley Jr., P.J., 2014c. Time-optimal path planning in dynamic flows using level set equations: theory and schemes. Ocean Dyn. 64 (10), 1373–1397.

Lolla, T., Ueckermann, M.P., Yigit, K., Haley, P.J., Lermusiaux, P.F.J., 2012. Path planning in time dependent flow fields using level set methods. In: Proceedings of the IEEE International Conference on Robotics and Automation, pp. 166–173.

Lu, P., Lermusiaux, P.F.J., 2016. Model learning in biogeochemical systems. Physica D.Preprint

MacKay, D.J., 2003. Information theory, inference and learning algorithms. Cambridge University Press, Cambridge, UK.

McLain, T.W., Beard, R.W., 1998. Successive galerkin approximations to the nonlinear optimal control of an underwater robotic vehicle. In: Proceedings of IEEE International Conference on Robotics and Automation, 1. IEEE, pp. 762–767.

Melchior, N.A., Simmons, R., 2007. Particle RRT for path planning with uncertainty. In: Proceedings of the IEEE International Conference on Robotics and Automation, 2007, pp. 1617–1624. doi:10.1109/ROBOT.2007.363555.

Michini, M., Hsieh, M.A., Forgoston, E., Schwartz, I.B., 2014. Robotic tracking of coherent structures in flows. IEEE Trans. Robot. 30 (3), 593–603. doi:10.1109/TRO.2013.2295655.

Murphy, K.P., 2012. Machine Learning: A Probabilistic Perspective. MIT press, Cambridge, MA.

Osher, S., Sethian, J.A., 1988. Fronts propagating with curvature-dependent speed: algorithms based on Hamilton–Jacobi formulations. J. Comput. Phys. 79 (1), 12–49.

Pedlosky, J., 1998. Ocean Circulation Theory. Springer-Verlag, Berlin.

Petres, C., Pailhas, Y., Patron, P., Petillot, Y., Evans, J., Lane, D., 2007. Path planning for autonomous underwater vehicles. IEEE Trans. Robot. 23 (2), 331–341.

Ramp, S.R., Davis, R.E., Leonard, N.E., Shulman, I., Chao, Y., Robinson, A.R., Marsden, J., Lermusiaux, P.F.J., Fratantoni, D.M., Paduan, J.D., Chavez, F.P., Bahr, F.L., Liang, S., Leslie, W., Li, Z., 2009. Preparing to predict: the second autonomous ocean sampling network (AOSN-II) experiment in the Monterey Bay. Deep Sea Res. Part II: Top. Stud. Oceanogr. 56 (3–5), 68–86.10.1016/j.dsr2.2008.08.013

Rao, D., Williams, S.B., 2009. Large-scale path planning for underwater gliders in ocean currents. In: Proceedings of Australasian Conference on Robotics and Automation, pp. 28–35.

Rhoads, B., Mezić, I., Poje, A., 2010. Minimum time feedback control of autonomous underwater vehicles. In: IEEE Conference on Decision and Control (CDC), 2010 49th. IEEE, pp. 5828–5834.

Rudnick, D.L., Davis, R.E., Eriksen, C.C., Fratantoni, D.M., Perry, M.J., 2004. Underwater gliders for ocean research. Mar. Technol. Soc. J. 38 (2), 73–84.

Sapsis, T.P., Lermusiaux, P.F.J., 2009. Dynamically orthogonal field equations for continuous stochastic dynamical systems. Phys. D: Nonlinear Phenom. 238 (23–24), 2347–2360.10.1016/j.physd.2009.09.017

Sapsis, T.P., Lermusiaux, P.F.J., 2012. Dynamical criteria for the evolution of the stochastic dimensionality in flows with uncertainty. Phys. D: Nonlinear Phenom. 241 (1), 60–76. doi:10.1016/j.physd.2011.10.001.

Schmidt, H., Bellingham, J.G., Johnson, M., Herold, D., Farmer, D., Pawlowicz, R., 1996. Real-time frontal mapping with AUVs in a coastal environment. In: Conference Proceedings of the Prospects for the 21st Century OCEANS '96. MTS/IEEE, 3, pp. 1094–1098.

Schofield, O., Glenn, S., Orcutt, J., Arrott, M., Meisinger, M., Gangopadhyay, A., Brown, W., Signell, R., Moline, M., Chao, Y., Chien, S., Thompson, D., Balasuriya, A., Lermusiaux, P.F.J., Oliver, M., 2010. Automated sensor networks to advance ocean science. Eos Trans. AGU 91 (39), 345–346. doi:10.1029/2010EO390001.

Schofield, O., Kohut, J., Aragon, D., Creed, L., Graver, J., Haldeman, C., Kerfoot, J., Roarty, H., Jones, C., Webb, D., et al., 2007. Slocum gliders: robust and ready. J. Field Robot. 24 (6), 473–485.

Sethian, J.A., 1999a. Fast marching methods. SIAM Rev. 41 (2), 199–235.

Sethian, J.A., 1999b. Level Set Methods and Fast Marching Methods: Evolving Interfaces in Computational Geometry, Fluid Mechanics, Computer Vision, and Materials Science. Cambridge University Press: Cambridge, U.K..

Sherman, J., Davis, R., Owens, W., Valdes, J., 2001. The autonomous underwater glider "spray". IEEE J. Ocean Eng. 26 (4), 437–446.

Sheu, P.C.-Y., Xue, Q., 1993. Intelligent Robotic Planning Systems. World Scientific Publishing, Singapore.

Simmonet, E., Dijkstra, H., Ghil, M., 2009. Bifurcation analysis of ocean, atmosphere, and climate models. in 'computational methods for the atmosphere and the oceans'. Handbook of Numerical Analysis. Elsevier, p. 187-229.

Soulignac, M., Taillibert, P., Rueher, M., 2009. Time-minimal path planning in dynamic current fields. In: Robotics and Automation, 2009. ICRA '09. IEEE International Conference on, pp. 2473–2479.

Stommel, H., 1989. The slocum mission. Oceanography 2 (1), 22–25.

Subramani, D.N., 2014. Energy Optimal Path Planning Using Stochastic Dynamically Orthogonal Level Set Equations. School of Engineering, Massachusetts Institute of Technology Master's thesis.

Subramani, D.N., Haley Jr., P.J., Lermusiaux, P.F.J., 2016. Energy-optimal path planning in the coastal ocean: Integrating re-analyses with stochastic dynamically orthogonal level-set optimization. J. Geophys. Res. Oceans. Submitted.

Subramani, D.N., Lolla, T., Haley Jr., P.J., Lermusiaux, P.F.J., 2015. A stochastic optimization method for energy-based path planning. In: Ravela, S., Sandu, A. (Eds.), DyDESS 2014. In: *LNCS*, 8964. Springer, pp. 1–12. doi:10.1007/978-3-319-25138-731.

Sun, W., Tsiotras, P., 2015. Pursuit evasion game of two players under an external flow field. In: American Control Conference (ACC), 2015. IEEE, pp. 5617–5622.

Tan, C.S., Sutton, R., Chudley, J., 2004. An incremental stochastic motion planning technique for autonomous underwater vehicles. In: Proceedings of IFAC Control Applications in Marine Systems Conference, pp. 483–488.

Thompson, D.R., Chien, S.A., Chao, Y., Li, P., Arrott, M., Meisinger, M., Balasuriya, A.P., Petillo, S., Schofield, O., 2009. Glider Mission Planning in a Dynamic Ocean Sensorweb. SPARK Workshop on Scheduling and Planning Applications. International Conference on Automated Planning and Scheduling.

Thompson, D.R., Chien, S.A., Chao, Y., Li, P., Cahill, B., Levin, J., Schofield, O., Balasuriya, A.P., Petillo, S., Arrott, M., Meisinger, M., 2010. Spatiotemporal path planning in strong, dynamic, uncertain currents. In: Proceedings of IEEE International Conference on Robotics and Automation, pp. 4778–4783.

Ueckermann, M.P., Lermusiaux, P.F.J., 2011. 2.29 Finite Volume MATLAB Framework Documentation. Technical Report. Massachusetts Institute of Technology, Cambridge, MA USA.

Ueckermann, M.P., Lermusiaux, P.F.J., Sapsis, T.P., 2013. Numerical schemes for dynamically orthogonal equations of stochastic fluid and ocean flows. J. Comput. Phys. 233, 272–294. doi:10.1016/j.jcp.2012.08.041.

Warren, C.W., 1990. A technique for autonomous underwater vehicle route planning. In: Proceedings of the Symposium on Autonomous Underwater Vehicle Technology, pp. 201–205.

Webb, D.C., Simonetti, P.J., Jones, C.P., 2001. Slocum: an underwater glider propelled by environmental energy. IEEE J. Ocean Eng. 26 (4), 447–452.

Wei, Q., 2015. Time-Optimal Planning in Uncertain Flow Fields Using Stochastic Dynamically Orthogonal Level Set Equations. BS Thesis. Department of Mechanical Engineering, Massachusetts Institute of Technology.

Witt, J., Dunbabin, M., 2008. Go with the flow: optimal auv path planning in coastal environments. In: Kim, J., Mahony, R. (Eds.), Proceedings of Australasian Conference on Robotics and Automation, pp. 86–94.

Yang, K., Gan, S., Sukkarieh, S., 2010. An efficient path planning and control algorithm for ruavs in unknown and cluttered environments. J. Intell. Robot. Syst. 57, 101–122. doi:10.1007/s10846-009-9359-1.

Zhang, W., Inanc, T., Ober-Blobaum, S., Marsden, J.E., 2008. Optimal trajectory generation for a glider in time-varying 2D ocean flows B-spline model. In: Proceedings of the IEEE International Conference on Robotics and Automation, pp. 1083–1088.